J. Fluid Mech. (2026), *vol.* 1028, A45, doi:10.1017/jfm.2026.11122

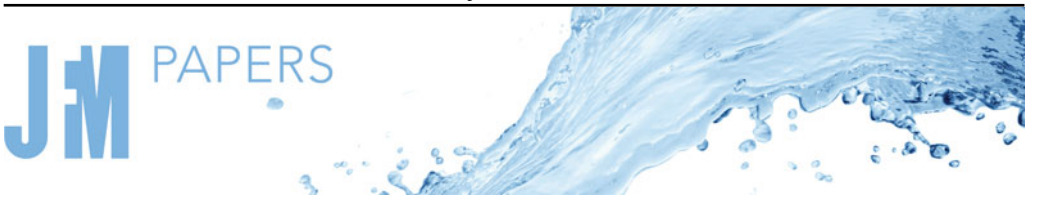

Linear stability of nanofluid boundary-layer flow over a flat plate

Christian Thomas[1], **Sharon O. Stephen**[2], **Jitesh S.B. Gajjar**[3] and **Paul T. Griffiths**[4]

[1]School of Mathematical and Physical Sciences, Macquarie University, Sydney, NSW 2109, Australia

[2]School of Mathematics and Statistics, University of Sydney, Sydney, NSW 2006, Australia

[3]Department of Mathematics, University of Manchester, Oxford Road, Manchester M13 9PL, UK

[4]Aston Fluids Group and School of Engineering & Innovation, Aston University, Birmingham B4 7ET, UK

Corresponding author: Christian Thomas, christian.thomas@mq.edu.au

(Received 15 August 2025; revised 9 November 2025; accepted 23 December 2025)

The linear stability of nanofluid boundary-layer flow over a flat plate is investigated using a two-phase formulation that incorporates the Brinkman (1952 *J. Chem. Phys.*, vol. **20**, pp. 571–581) model for viscosity along with Brownian motion (BM) and thermophoresis (TP), building upon the earlier work of Buongiorno (2006 *J. Heat Transfer*, vol. **128**, pp. 240–250). Solutions to the steady boundary-layer equations reveal a thin nanoparticle concentration layer near the plate surface, with a characteristic thickness of $O(Re^{-1/2}Sc^{-1/3})$, for a Reynolds number Re and Schmidt number Sc. When BM and TP are neglected, the governing equations reduce to the standard Blasius formulation for a single-phase fluid, and the nanoparticle concentration layer disappears, resulting in a uniform concentration across the boundary layer. Neutral stability curves and critical conditions for the onset of the Tollmien–Schlichting (TS) wave are computed for a range of nanoparticle materials and volume concentrations. Results indicate that while the effects of BM and TP are negligible, the impact of nanoparticle density is significant. Denser nanoparticles, such as silver and copper, destabilise the TS wave, whereas lighter nanoparticles, like aluminium and silicon, establish a small stabilising effect. Additionally, the viscosity model plays a crucial role, with alternative formulations leading to different stability behaviour. Finally, a high Reynolds number asymptotic analysis is undertaken for the lower branch of the neutral stability curve.

Key words: boundary layers, boundary layer stability, instability

1. Introduction

This paper is concerned with the influence of nanofluids on the linear stability of disturbances in the boundary-layer flow over a flat plate. Nanofluids are fluids containing nanoscale particles ranging from 1 to 100 nm, dispersed in a base fluid like water. These nanoparticles, composed of metal-based or carbon-based materials, enhance the thermal properties of the base fluid.

Since the seminal work of Choi (1995), nanofluids have received considerable interest, with a rapid growth in annual publications (Taylor *et al.* 2013). Numerous studies have investigated the thermal benefits of nanofluids, including comprehensive reviews by Das, Choi & Patel (2006), Wang & Mujumdar (2008*a*,*b*), Kakaç & Pramuanjaroenkij (2009), Mahbubul, Saidur & Amalina (2012) and Mishra *et al.* (2014). These thermal improvements have led to a wide range of heat transfer applications, including cooling systems for automotive engines (Sidik, Yazid & Mamat 2015), electronics (Bahiraei & Heshmatian 2018), nuclear systems (Buongiorno & Hu 2009), solar thermal systems (Khullar *et al.* 2012), biomedical processes (Sheikhpour *et al.* 2020) and industrial applications (Wong & Leon 2010).

Despite the ongoing interest in nanofluids for their thermal benefits, relatively few investigations have examined the impact of nanofluids on the hydrodynamic stability of flows. This study aims to address this knowledge gap by investigating the capabilities of nanofluids in controlling laminar–turbulent transition processes.

1.1. *Modelling nanofluid flows*

A key aspect of modelling nanofluid flows is how suspended nanoparticles modify the fluid's effective viscosity. For dilute suspensions of rigid, spherical particles, Einstein (1906) showed that the dynamic viscosity increases linearly with the nanoparticle volume concentration ϕ. He defined the effective dynamic viscosity as

$$\mu^* = \mu^*_{bf}(1 + 2.5\phi), \tag{1.1}$$

where μ^*_{bf} is the dynamic viscosity of the base fluid. Since Einstein's work, many viscosity models have been proposed to account for additional factors, including particle shape, size distribution and particle–particle interactions. Batchelor (1977) extended Einstein's formula to include the effects of Brownian motion (BM) (that is, the random movement of nanoparticles in a base fluid), while Brinkman (1952) proposed a semiempirical correlation valid for nanoparticle volume concentrations up to approximately 4 %. (The formulae for the Batchelor and Brinkman models are given in the subsequent section.) Comprehensive reviews of nanofluid viscosity models, including experimental and theoretical developments, are provided by Wang & Mujumdar (2008*a*) and Mishra *et al.* (2014).

Another key aspect of nanofluid modelling is the treatment of the fluid either as a single-phase or a two-phase flow. Single-phase models treat the nanofluid as a homogeneous mixture with effective properties, while two-phase models account for interactions between the base fluid and nanoparticles. The latter approach can capture additional effects such as particle migration, BM and thermophoresis (TP) (that is, the movement of nanoparticles in a base fluid due to a temperature gradient). Moreover, two-phase flow models include a continuity equation for the nanoparticle volume concentration.

The steady boundary-layer flow over a flat plate has been investigated by Buongiorno (2006), Avramenko, Blinov & Shevchuk (2011) and MacDevette, Myers & Wetton (2014). These studies employed the Brinkman (1952) model to describe the nanofluid viscosity and incorporated BM and TP into the governing equations. To simplify the analysis,

Buongiorno (2006) assumed the flow to be incompressible, even though modelling the nanofluid as a two-component mixture implies a non-constant density. Despite this apparent inconsistency, Buongiorno (2006) showed that the effects of BM and TP are negligible in nanofluids and attributed the observed heat transfer benefits to the improved thermophysical properties of the nanoparticles.

While acknowledging that BM and TP effects are weak, Avramenko *et al.* (2011) derived boundary-layer equations similar to those of Blasius (1908). However, despite accounting for compressibility effects in the base flow, the study implemented several simplifying assumptions. Notably, the incompressible flow condition was applied to the nanoparticle continuity equation (see equations (1)–(4) of Avramenko *et al.* (2011)). Additionally, the coefficients for BM and TP, defined below in (2.7), were treated as constants, even though they depend on temperature and nanoparticle volume concentration, respectively. Yet despite these simplifications, Avramenko *et al.* (2011) demonstrated that a thin concentration layer forms near the plate surface. This concentration layer modifies the velocity and temperature fields in the near-wall region, which may, in turn, influence instabilities within the boundary layer.

Both Buongiorno (2006) and Avramenko *et al.* (2011) confirmed that heat transfer, measured by the Nusselt number Nu, is enhanced as the nanoparticle volume concentration ϕ increases. In contrast, MacDevette *et al.* (2014), who also confirmed that BM and TP are negligible, observed a reduced heat transfer coefficient as ϕ increases. They attributed the discrepancy with earlier studies to differences in the definition of the heat transfer coefficient.

The study of nanofluids in boundary-layer flows has been extended to include flows past vertical plates (Kuznetsov & Nield 2010), planar wall jets (Turkyilmazoglu 2016), stretching sheets (Reddy *et al.* 2025) and the flow due to a rotating-disk (Bachok, Ishak & Pop 2011; Turkyilmazoglu 2014; Mehmood & Usman 2018), with these studies reporting enhanced heat transfer due to the introduction of nanoparticles.

Using triple-deck theory, Wasaif (2023) modelled a nanofluid boundary-layer flow past a hump, on an otherwise flat plate. The study demonstrated that a nanofluid can suppress the region of flow separation along the rear side of the bump. More recently, Gandhi, Nepomnyashchy & Oron (2025) examined thermosolutal instabilities in a nanofluid layer with a deformable surface, showing how the Soret effect and thermal properties influence instability characteristics.

1.2. *Linear stability studies*

The linear stability of the incompressible Blasius boundary layer has been extensively studied, beginning with the seminal investigations of Tollmien (1933) and Schlichting (1933), which led to the Orr–Sommerfeld equation. These studies employed the parallel flow approximation, where the flow is assumed to be unidirectional and depends only on the wall-normal coordinate. The theoretical predictions for the Tollmien–Schlichting (TS) wave were subsequently confirmed experimentally by Schubauer & Skramstad (1947). Further theoretical and experimental insights into the stability of TS waves were reported by Jordinson (1970), Barry & Ross (1970), Ross *et al.* (1970) and Gaster (1974), amongst many others.

Using triple-deck theory, Smith (1979) undertook an asymptotic, high Reynolds number Re analysis to describe the structure of the lower branch of the neutral stability curve in the Blasius boundary layer (Lin 1955). The triple-deck framework consists of three layers: an upper deck, representing the inviscid outer flow and spans a thickness of $O(Re^{-3/8})$; a main deck, corresponding to the boundary layer, with thickness $O(Re^{-4/8})$; and a lower

deck, a thin viscous sublayer of thickness $O(Re^{-5/8})$, where viscous–inviscid interactions are dominant. (A formal definition for the Reynolds number Re is given below in (2.15*a*)) A subsequent study by Bodonyi & Smith (1981) employed a multideck approach to derive the corresponding structure of the upper branch of the neutral stability curve. Later, Smith (1989) extended the asymptotic analysis of the lower branch to compressible boundary-layer flows.

Building on earlier studies, Bertolotti, Herbert & Spalart (1992) employed parabolised stability equations to investigate both the linear and nonlinear development of TS waves in the Blasius boundary layer. Healey (1995) compared the asymptotic scalings of the lower and upper branches with solutions from the Orr–Sommerfeld equation and experimental observations. More recently, both asymptotic and numerical approaches have been utilised to model the effects of non-Newtonian viscosity (Griffiths, Gallacher & Stephen 2016) and temperature-dependent viscosity (Miller *et al.* 2018) on the stability of the Blasius boundary layer.

To the authors' knowledge, there are only two previous studies concerning the linear stability of nanofluid boundary-layer flows. The first, by Turkyilmazoglu (2020), considered the application of nanofluids to several configurations, including the Kelvin–Helmholtz instability, Rayleigh–Bénard convection, instabilities in rotating disk flows and instabilities in the boundary-layer flow over a flat plate. Turkyilmazoglu modelled the latter flow as a single-phase flow, with quantities scaled on nanofluid properties, i.e. the combined characteristics of the base fluid and nanoparticles. This approach led to a Reynolds number based on nanofluid characteristics and a base flow described by the Blasius equation. The findings suggest that the Reynolds number of the nanofluid can be predicted using the Reynolds number of the base fluid. Moreover, results indicate that denser nanoparticle materials, like silver (Ag), stabilise the flow, while less dense nanoparticle materials, such as alumina (Al_2O_3), destabilise the flow at sufficiently larger volume concentrations ϕ. However, the rationale for scaling quantities on nanofluid characteristics is unclear, as the resulting Reynolds number changes as the nanoparticle volume concentration ϕ increases, making it difficult to compare solutions. In the following study, the nanofluid flow is modelled as a two-phase flow that includes diffusion effects due to BM and TP, with the Reynolds number based on the base fluid properties to facilitate comparisons across different nanoparticle materials and variable ϕ.

A second study, by Laouer *et al.* (2024), examined the linear stability of a nanofluid flow past stationary and moving wedges. Similar to Turkyilmazoglu (2020), Laouer *et al.* (2024) employed a single-phase flow approach, using the base flow formulation of Yacob, Ishak & Pop (2011) and a linear stability analysis that simplifies to the standard Orr–Sommerfeld equation for a regular fluid. Laouer *et al.* (2024) showed that, for a nanofluid flow over a stationary wedge due to a favourable pressure gradient, increasing the volume concentration ϕ leads to a destabilising effect. Additionally, Laouer and coworkers suggest that heavier nanoparticle materials, such as copper (Cu), have a stabilising effect, while lighter materials, like titanium oxide (TiO_2) and Al_2O_3, destabilise the flow. However, this latter finding appears to contradict the results presented in figure 8 of their paper, which shows that Cu nanoparticles shift neutral stability curves to the left and smaller Reynolds numbers, while TiO_2 and Al_2O_3 nanoparticles shift neutral stability curves to the right and higher Reynolds numbers.

1.3. *Outline of paper*

The following study investigates the linear stability of nanofluid flow over a flat plate using a two-phase flow model that accounts for BM and TP. This model addresses

the inconsistencies in previous single-phase studies and provides a physically consistent method for analysing stability trends. Both numerical and asymptotic analyses are undertaken to compute neutral stability curves and examine the lower branch behaviour at high Reynolds numbers. The most amplified TS disturbances appear near the lower branch of the neutral curve, and this, combined with the need to validate our numerical solutions, motivates the analysis of the lower rather than the upper branch.

The remainder of this paper is outlined as follows. The governing equations are introduced in the next section, followed by the steady, two-dimensional boundary-layer equations and its solutions in § 3. Linear stability results for three-dimensional disturbances, including neutral stability curves and critical conditions, are presented in § 4. An asymptotic analysis of the lower branch is provided in § 5. Conclusions are given in § 6.

2. Governing equations

2.1. *Model*

Consider the flow of a nanofluid over a semi-infinite flat plate with free stream velocity U_∞^*. (Here, an asterisk denotes dimensional quantities.) The model is given in Cartesian coordinates $\boldsymbol{x}^* = (x^*, y^*, z^*)$, where x^* measures the distance along the surface of the flat plate, y^* denotes the direction normal to the plate and z^* the spanwise direction. Consequently, the governing system of equations comprise the continuity, momentum and energy equations for fluid motion (Ruban & Gajjar 2014), along with a continuity equation for the nanoparticles (Buongiorno 2006; Avramenko *et al.* 2011; MacDevette *et al.* 2014),

$$\frac{\partial \rho^*}{\partial t^*} + \nabla^* \cdot (\rho^* \boldsymbol{u}^*) = 0, \tag{2.1a}$$

$$\rho^* \left(\frac{\partial \boldsymbol{u}^*}{\partial t^*} + (\boldsymbol{u}^* \cdot \nabla^*)\boldsymbol{u}^* \right) = -\nabla^* p^* + \nabla^* \cdot \left(\mu^* \left(\nabla^* \boldsymbol{u}^* + \left(\nabla^* \boldsymbol{u}^*\right)^T - \frac{2}{3} \nabla^* \cdot \boldsymbol{u}^* \boldsymbol{I} \right) \right), \tag{2.1b}$$

$$\rho^* \left(\frac{\partial \left(c^* T^*\right)}{\partial t^*} + (\boldsymbol{u}^* \cdot \nabla^*) \left(c^* T^*\right) \right) = \nabla^* \cdot \left(k^* \nabla^* T^*\right) + (\rho^* c^*)_{np} \left(D_B^* \nabla^* \phi + D_T^* \frac{\nabla^* T^*}{T^*} \right) \cdot \nabla^* T^*, \tag{2.1c}$$

$$\frac{\partial \phi}{\partial t^*} + \nabla^* \cdot (\phi \boldsymbol{u}^*) = \nabla^* \cdot \left(D_B^* \nabla^* \phi + D_T^* \frac{\nabla^* T^*}{T^*} \right), \tag{2.1d}$$

for a velocity $\boldsymbol{u}^* = (u^*, v^*, w^*)$, pressure p^*, temperature T^* and dimensionless nanoparticle volume concentration ϕ. Here, $\boldsymbol{I}$ is the identity matrix.

The density of the nanofluid ρ^* is defined using the law of mixtures as

$$\rho^* = (1 - \phi)\rho_{bf}^* + \phi \rho_{np}^*, \tag{2.2}$$

where subscripts bf and np represent quantities associated with the base fluid and nanoparticles, respectively. In addition,

$$\rho^* c^* = (1 - \phi)(\rho^* c^*)_{bf} + \phi (\rho^* c^*)_{np}, \tag{2.3}$$

where c^* denotes the specific heat capacity of the nanofluid, while the thermal conductivity of the nanofluid k^* is given by the Maxwell (1881) model:

$$k^* = \left(\frac{k^*_{np} + 2k^*_{bf} + 2\phi\left(k^*_{np} - k^*_{bf}\right)}{k^*_{np} + 2k^*_{bf} - \phi\left(k^*_{np} - k^*_{bf}\right)} \right) k^*_{bf}. \tag{2.4}$$

Alternative models for k^* may be considered as discussed in Wang & Mujumdar (2008*a*).

The dynamic viscosity of the nanofluid μ^*, used throughout the subsequent study, is given by the Brinkman (1952) model,

$$\mu^* = \frac{\mu^*_{bf}}{(1-\phi)^{2.5}}, \tag{2.5}$$

for a base fluid dynamic viscosity μ^*_{bf}. The Brinkman relation is known to under predict the dynamic viscosity for $\phi > 0.01$ (MacDevette *et al.* 2014). However, for theoretical purposes and to demonstrate trends, here we consider nanoparticle volume concentrations ϕ up to 10 % of the fluid volume. Similar to the thermal conductivity k^*, alternative models may be considered for the dynamic viscosity μ^*, as listed in Wang & Mujumdar (2008*a*) and Mishra *et al.* (2014), which encompass properties such as the size and distribution of nanoparticles. For instance, Batchelor (1977) modelled the dynamic viscosity as

$$\mu^* = \mu^*_{bf}\left(1 + 2.5\phi + 6.2\phi^2\right), \tag{2.6a}$$

whereas Pak & Cho (1998) and Maiga *et al.* (2004) obtained the correlations

$$\mu^* = \mu^*_{bf}\left(1 + 39.11\phi + 533.9\phi^2\right) \quad \text{and} \quad \mu^* = \mu^*_{bf}\left(1 + 7.3\phi + 123\phi^2\right), \tag{2.6b,c}$$

for nanofluids inside circular pipes and tubes, respectively.

The latter two terms of (2.1*c*) and the two terms on the right-hand side of (2.1*d*) model the respective effects of BM and TP, with coefficients

$$D^*_B = \frac{k^*_B T^*}{3\pi \mu^*_{bf} d^*_{np}} \equiv C^*_B T^* \quad \text{and} \quad D^*_T = \frac{\beta_T \mu^*_{bf} \phi}{\rho^*_{bf}} \equiv C^*_T \phi. \tag{2.7a,b}$$

Here, k^*_B denotes the Boltzmann constant, d^*_{np} the diameter of the nanoparticles and the proportionality constant

$$\beta_T = 0.26 \frac{k^*_{bf}}{2k^*_{bf} + k^*_{np}}, \tag{2.8}$$

as given in McNab & Meisen (1973), Buongiorno (2006) and MacDevette *et al.* (2014).

The nanofluid flow is subject to the no-slip condition and the fixed temperature condition on the plate surface

$$\boldsymbol{u}^* = 0 \quad \text{and} \quad T^* = T^*_w \quad \text{on} \quad y^* = 0, \tag{2.9a,b}$$

where T^*_w denotes the constant wall temperature. (Here, a subscript w references wall conditions.) In addition,

$$D^*_B \frac{\partial \phi}{\partial y^*} + \frac{D^*_T}{T^*} \frac{\partial T^*}{\partial y^*} = 0 \quad \text{on} \quad y^* = 0, \tag{2.9c}$$

following Avramenko *et al.* (2011), which imposes that the total flux of nanoparticles at the plate surface is zero. Finally, in the far-field, the flow is subject to the free stream conditions

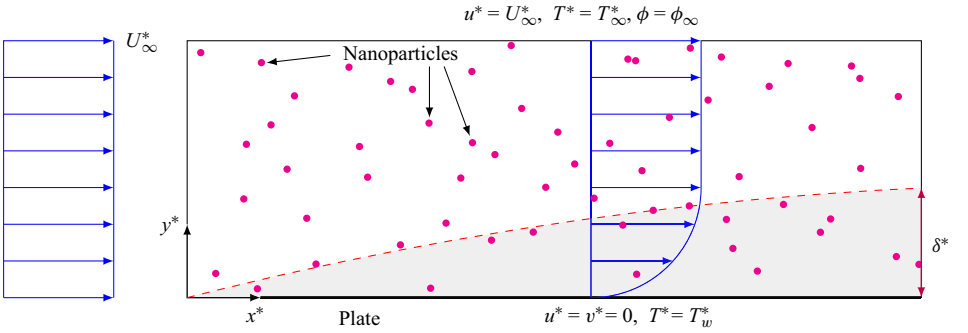

Figure 1. Diagram of a nanofluid flow, composed of a base fluid (bf) and nanoparticles (np) over a flat plate. Here, δ^* represents the boundary-layer thickness.

$$u^* \to U^*_\infty, \quad v^* \to 0, \quad w^* \to 0, \quad p^* \to p^*_\infty, \quad T^* \to T^*_\infty, \quad \phi \to \phi_\infty \quad \text{as} \quad y^* \to \infty, \tag{2.10a–f}$$

where p^*_∞, T^*_∞ and ϕ_∞ denote the free stream pressure, the free stream temperature and the dimensionless free stream nanoparticle volume concentration, respectively. Figure 1 shows a schematic diagram of the nanofluid flow over a flat plate.

2.2. *Non-dimensionalisation*

The governing system of equations (2.1) are non-dimensionalised by setting

$$\boldsymbol{x}^* = L^*\boldsymbol{x}, \quad \boldsymbol{u}^* = U^*_\infty \boldsymbol{u}, \quad t^* = L^* t/U^*_\infty, \quad p^* = p^*_\infty + \rho^*_{bf} U^{*2}_\infty p, \quad T^* = T^*_\infty T, \quad \rho^* = \rho^*_{bf}\rho, \quad \mu^* = \mu^*_{bf}\mu, \quad c^* = c^*_{bf}c, \quad k^* = k^*_{bf}k, \tag{2.11a–i}$$

for a characteristic length scale L^*. Consequently, (2.1) becomes

$$\frac{\partial \rho}{\partial t} + \nabla \cdot (\rho \boldsymbol{u}) = 0, \tag{2.12a}$$

$$\rho\left(\frac{\partial \boldsymbol{u}}{\partial t} + (\boldsymbol{u}\cdot\nabla)\boldsymbol{u}\right) = -\nabla p + \frac{1}{Re}\nabla\cdot\left(\mu\left(\nabla\boldsymbol{u} + (\nabla\boldsymbol{u})^T - \frac{2}{3}\nabla\cdot\boldsymbol{u}\boldsymbol{I}\right)\right), \tag{2.12b}$$

$$\rho\left(\frac{\partial\,(cT)}{\partial t} + (\boldsymbol{u}\cdot\nabla)\,(cT)\right) = \frac{1}{RePr}\nabla\cdot(k\nabla T) + \frac{1}{RePrLe}\left(T\nabla\phi + \frac{\phi\nabla T}{N_{BT}T}\right)\cdot\nabla T, \tag{2.12c}$$

$$\frac{\partial \phi}{\partial t} + \nabla\cdot(\phi\boldsymbol{u}) = \frac{1}{ReSc}\nabla\cdot\left(T\nabla\phi + \frac{\phi\nabla T}{N_{BT}T}\right), \tag{2.12d}$$

where

$$\rho = 1 + (\hat{\rho} - 1)\phi \quad \text{for} \quad \hat{\rho} = \frac{\rho^*_{np}}{\rho^*_{bf}}, \tag{2.13a}$$

$$\rho c = 1 + (\hat{\rho}\hat{c} - 1)\phi \quad \text{for} \quad \hat{\rho}\hat{c} = \frac{(\rho^* c^*)_{np}}{(\rho^* c^*)_{bf}}, \tag{2.13b}$$

$$k = \left(\frac{\hat{k} + 2 + 2(\hat{k} - 1)\phi}{\hat{k} + 2 - (\hat{k} - 1)\phi}\right) \quad \text{for} \quad \hat{k} = \frac{k^*_{np}}{k^*_{bf}}. \tag{2.13c}$$

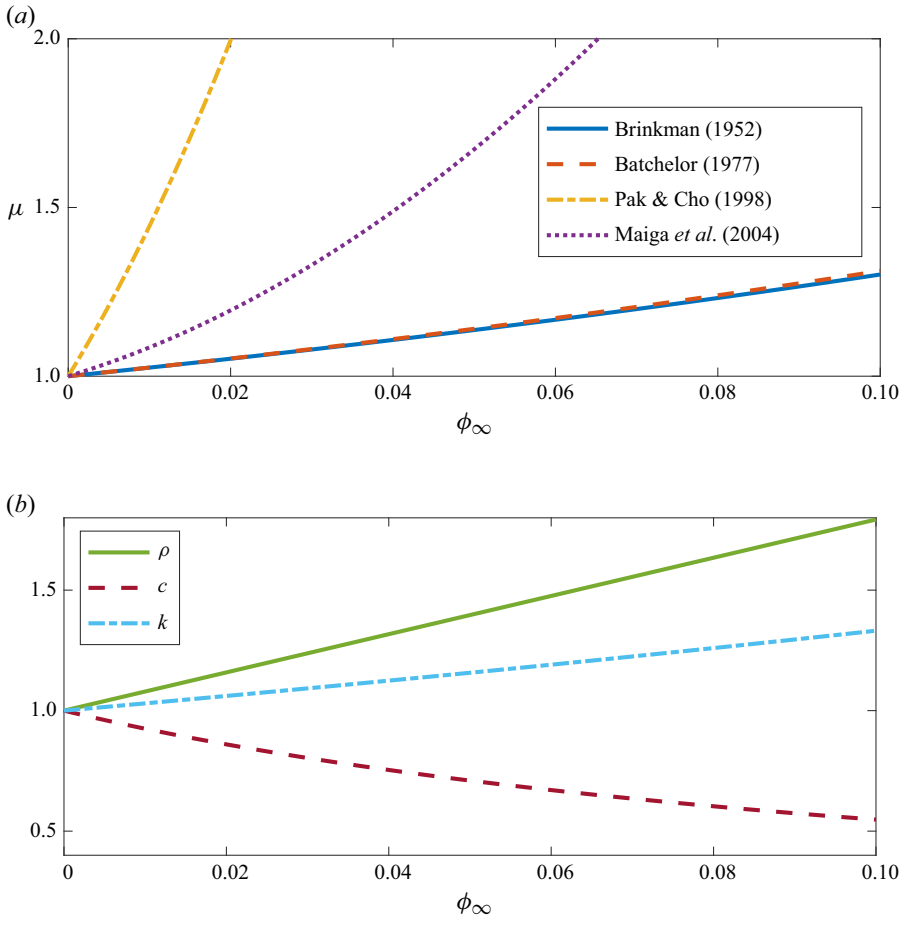

Figure 2. (*a*) Non-dimensional dynamic viscosity μ as a function of ϕ_∞, for the Brinkman (1952), Batchelor (1977), Pak & Cho (1998) and Maiga *et al.* (2004) models. (*b*) Non-dimensional density ρ, specific heat capacity c and thermal conductivity k as a function of ϕ_∞, for Cu nanoparticles in water. Refer to table 1 for fluid and nanoparticle properties.

Moreover, in the case of the Brinkman (1952) viscosity model, given by (2.5), the non-dimensional dynamic viscosity is given as

$$\mu = \frac{1}{(1-\phi)^{2.5}}. \tag{2.14}$$

Similar representations for μ are given for the Batchelor (1977), Pak & Cho (1998) and Maiga *et al.* (2004) models.

Figure 2 compares the four models of the non-dimensional dynamic viscosity μ along with the non-dimensional density ρ, thermal conductivity k and specific heat capacity c for Cu nanoparticles in water (see table 1 for thermophysical properties). These quantities are plotted as functions of the free stream nanoparticle volume concentration ϕ_∞. As ϕ_∞ increases, the Brinkman and Batchelor viscosity models show a similar rate of increase, while the Pak–Cho and Maiga viscosity models exhibit a more rapid increase. In addition, ρ also increases with ϕ_∞. Furthermore, k increases, improving the flows heat transfer

https://doi.org/10.1017/jfm.2026.11122 Published online by Cambridge University Press

	ρ^* (kg m^{-3})	μ^* (kg (ms)$^{-1}$)	k^* (W (mK)$^{-1}$)	c^* (J (kgK)$^{-1}$)	$\hat{\rho}$	$\hat{k}$	$\hat{c}$	β_T	Le	Sc	N_{BT}
Water	1000	0.001	0.61	4180	–	–	–	–	–	–	–
Ag	10 500	—	430	235	10.50	704.9	0.0562	0.00037	11 250	45 509	0.0597
Cu	8933	—	400	385	8.93	655.7	0.0921	0.00040	8072	45 509	0.0556
Copper oxide (CuO)	6320	—	77	532	6.32	126.2	0.1273	0.00203	8257	45 509	0.0108
Al_2O_3	3950	—	35	800	3.95	57.4	0.1914	0.00438	8785	45 509	0.0050
TiO_2	4250	—	8.95	686	4.25	14.7	0.1641	0.01559	9522	45 509	0.0014
Al	2710	—	235	904	2.71	385.2	0.2163	0.00067	11 332	45 509	0.0327
Si	2330	—	150	710	2.33	245.9	0.1699	0.00105	16 781	45 509	0.0210

Table 1. Thermophysical properties of water and various materials used for nanoparticles, as given in Buongiorno (2006), Wang & Mujumdar (2008*a*), Bachok *et al.* (2011), MacDevette *et al.* (2014), Turkyilmazoglu (2014, 2020) and at https://periodictable.com/Elements. Here, free stream temperature $T_\infty^* = 300$ K, nanoparticle diameter $d_{np}^* = 20$ nm and Prandtl number $Pr = 6.85$. The ratios $\hat{\rho}$, $\hat{k}$ and $\hat{c}$ are based on water as the base fluid.

capability, while c exhibits a reduction, causing temperature changes within the flow to occur more rapidly.

The dimensionless Reynolds, Prandtl, Lewis and Schmidt numbers are defined as

$$Re = \frac{U^*_\infty L^* \rho^*_{bf}}{\mu^*_{bf}}, \qquad Pr = \frac{\mu^*_{bf} c^*_{bf}}{k^*_{bf}}, \tag{2.15a,b}$$

$$Le = \frac{k^*_{bf}}{(\rho^* c^*)_{np} C^*_B T^*_\infty}, \qquad Sc = \frac{\mu^*_{bf}}{\rho^*_{bf} C^*_B T^*_\infty}, \tag{2.15c,d}$$

while the ratio of BM to TP is given as

$$N_{BT} = \frac{C^*_B T^*_\infty}{C^*_T}. \tag{2.16}$$

Finally, the boundary conditions (2.9) on the plate surface are recast as

$$\boldsymbol{u} = 0 \quad \text{and} \quad T = T_w \left(\equiv \frac{T^*_w}{T^*_\infty} \right) \quad \text{on} \quad y = 0, \tag{2.17a,b}$$

and

$$T \frac{\partial \phi}{\partial y} + \frac{\phi}{N_{BT} T} \frac{\partial T}{\partial y} = 0 \quad \text{on} \quad y = 0, \tag{2.17c}$$

while the boundary conditions (2.10) in the free stream are given as

$$\begin{aligned} &u \to 1, \qquad v \to 0, \qquad w \to 0, \\ &p \to 0, \qquad T \to 1, \qquad \phi \to \phi_\infty \qquad \text{as} \quad y \to \infty. \end{aligned} \tag{2.18a–f}$$

Table 1 presents the thermophysical properties of various materials used for nanoparticles. The non-dimensional ratios $\hat{\rho}$, $\hat{k}$ and $\hat{c}$ are based on water as the base fluid, where the Prandtl number $Pr = 6.85$, while the Lewis number Le, the Schmidt number Sc and the ratio N_{BT} are given for the free stream temperature $T^*_\infty = 300\,\text{K}$ and the nanoparticle diameter $d^*_{np} = 20\,\text{nm}$. Both Le and Sc are of the order 10^4 for all materials listed in table 1.

3. Steady boundary-layer flow

3.1. *Boundary-layer equations*

Following the derivation of Ruban (2017), the steady, two-dimensional boundary-layer equations are obtained by assuming a zero pressure gradient, setting $w = 0$, and considering solutions that are independent of the z-direction and time t. On introducing the Prandtl boundary-layer transformation

$$y = Re^{-1/2} Y, \tag{3.1}$$

with

$$\begin{aligned} &u(x, y) = U_B(x, Y), \quad v(x, y) = Re^{-1/2} V_B(x, Y), \\ &T(x, y) = T_B(x, Y), \quad \phi(x, y) = \phi_B(x, Y), \\ &\mu(x, y) = \mu_B(x, Y), \quad \rho(x, y) = \rho_B(x, Y), \\ &c(x, y) = c_B(x, Y), \quad k(x, y) = k_B(x, Y), \end{aligned} \tag{3.2a–h}$$

and letting $Re \to \infty$, the non-dimensional governing equations (2.12) become

$$\frac{\partial(\rho_B U_B)}{\partial x} + \frac{\partial(\rho_B V_B)}{\partial Y} = 0, \tag{3.3a}$$

$$\rho_B \left(U_B \frac{\partial U_B}{\partial x} + V_B \frac{\partial U_B}{\partial Y} \right) = \frac{\partial}{\partial Y} \left(\mu_B \frac{\partial U_B}{\partial Y} \right), \tag{3.3b}$$

$$\rho_B \left(U_B \frac{\partial(c_B T_B)}{\partial x} + V_B \frac{\partial(c_B T_B)}{\partial Y} \right) = \frac{1}{Pr} \frac{\partial}{\partial Y} \left(k_B \frac{\partial T_B}{\partial Y} \right) + \frac{1}{Pr\, Le} \left(T_B \frac{\partial \phi_B}{\partial Y} \frac{\partial T_B}{\partial Y} + \frac{\phi_B}{N_{BT} T_B} \left(\frac{\partial T_B}{\partial Y} \right)^2 \right), \tag{3.3c}$$

$$\frac{\partial(\phi_B U_B)}{\partial x} + \frac{\partial(\phi_B V_B)}{\partial Y} = \frac{1}{Sc} \frac{\partial}{\partial Y} \left(T_B \frac{\partial \phi_B}{\partial Y} + \frac{\phi_B}{N_{BT} T_B} \frac{\partial T_B}{\partial Y} \right). \tag{3.3d}$$

A self-similar solution is then sought using the similarity variable $\eta = Y/\sqrt{x}$, coupled with the Dorodnitsyn–Howarth transformation

$$\xi = \int_0^\eta \rho(\hat{\eta})\, \mathrm{d}\hat{\eta}, \tag{3.4}$$

with

$$\begin{aligned} U_B(x, Y) &= f'(\xi), \quad & V_B(x, Y) &= \frac{1}{2\sqrt{x}} \left(\eta f' - \frac{f}{\rho} \right), \\ T_B(x, Y) &= \theta(\xi), \quad & \phi_B(x, Y) &= \varphi(\xi), \\ \mu_B(x, Y) &= \mu(\xi), \quad & \rho_B(x, Y) &= \rho(\xi), \\ c_B(x, Y) &= c(\xi), \quad & k_B(x, Y) &= k(\xi). \end{aligned} \tag{3.5a–h}$$

(For notational simplicity, μ, ρ, c and k are reused to denote their similarity profiles.) Consequently, the following boundary-layer equations are derived:

$$2\left(\rho \mu f''\right)' + f f'' = 0, \tag{3.6a}$$

$$2\left(\rho k \theta'\right)' + Prf\,(c\theta)' + \frac{2\rho\theta'}{Le} \left(\theta\varphi' + \frac{\varphi\theta'}{N_{BT}\theta} \right) = 0, \tag{3.6b}$$

$$\frac{2\rho^2}{Sc} \left(\rho \left(\theta\varphi' + \frac{\varphi\theta'}{N_{BT}\theta} \right) \right)' + f\varphi' = 0, \tag{3.6c}$$

subject to the boundary conditions

$$f = f' = 0,\ \theta = T_w \quad \text{on} \quad \xi = 0, \tag{3.6d-f}$$

$$\theta\varphi' + \frac{\varphi\theta'}{N_{BT}\theta} = 0 \quad \text{on} \quad \xi = 0 \tag{3.6g}$$

and

$$f' \to 1, \quad \theta \to 1, \quad \varphi \to \phi_\infty \quad \text{as} \quad \xi \to \infty, \tag{3.6h–j}$$

where a prime denotes differentiation with respect to ξ.

3.2. *Boundary-layer simplifications*

In the limits $Le \to \infty$ and $Sc \to \infty$, (3.6c) simplifies to $\varphi' = 0$, implying $\varphi = \phi_\infty$ everywhere. Consequently, μ, ρ, c and k are constants, and the boundary-layer equations

(3.6*a*) and (3.6*b*) reduces to

$$2\rho\mu f''' + ff'' = 0 \quad \text{and} \quad 2\rho\mu\theta'' + \widehat{Pr} f\theta' = 0, \tag{3.7a,b}$$

where $\widehat{Pr} = \mu c Pr/k$.

A further simplification of the boundary-layer equations is obtained by introducing

$$p = \rho\hat{p}, \quad T = 1 + (T_w - 1)\widehat{T}, \quad \widehat{Re} = \frac{\rho}{\mu} Re = \frac{U_\infty^* L^* \rho^*}{\mu^*}, \tag{3.8a–c}$$

into the governing (2.12) and following the procedure outlined in § 3.1 with $\widehat{Re} \to \infty$, to give

$$2f''' + ff'' = 0 \quad \text{and} \quad 2\widehat{\theta}'' + \widehat{Pr} f\widehat{\theta}' = 0, \tag{3.9a,b}$$

subject to the boundary conditions

$$f = f' = 0, \ \widehat{\theta} = 1 \quad \text{on} \quad \xi = 0, \tag{3.9c–e}$$

and

$$f' \to 1, \quad \widehat{\theta} \to 0, \quad \text{as} \quad \xi \to \infty. \tag{3.9f,g}$$

Here, the similarity solution $\widehat{\theta}(\xi) = \widehat{T}(x, y)$, with ρ^* and μ^* representing the nanofluid density (2.2) and viscosity (2.5), respectively. The rescaling in (3.8) absorbs the density and viscosity, removing them from the governing equations. Consequently, the equations simplify to the standard Blasius formulation with a modified Prandtl number $\widehat{Pr}$ and Reynolds number $\widehat{Re}$ based on the nanofluid quantities, allowing the nanofluid flow to be modelled as a single-phase fluid. Thus, in this simplified formulation, the flow characteristics are identical to those obtained for the standard Blasius flow, irrespective of the nanofluid quantities. Hence, in the absence of BM and TP, the Reynolds number of the nanofluid flow Re is given in terms of $\widehat{Re}$ as $Re = \mu\widehat{Re}/\rho$. A detailed description of the Navier–Stokes equations in the absence of BM and TP, leading to the derivation of (3.9), is given in Appendix A.

3.3. *Boundary-layer solutions*

On the left-hand side of figure 3, the steady streamwise velocity $U_B = f'(\xi)$, temperature $T_B = \theta(\xi)$ and nanoparticle volume concentration $\phi_B = \varphi(\xi)$ are plotted for five values of ϕ_∞ and the wall temperature $T_w = 2$. Similar profiles are obtained for other values of T_w. The solid, dashed and chain lines represent solutions of the full boundary-layer equations (3.6) for Cu nanoparticles in water (see table 1 for thermophysical properties). A thin concentration layer develops in the ϕ_B profile, consistent with the observations of Avramenko *et al.* (2011), which alters the near-wall behaviour of the velocity and temperature profiles. This behaviour is most clearly illustrated on the right-hand side of figure 3, which plots the profiles $U_B' = f''(\xi)$, $T_B' = \theta'(\xi)$ and $\phi_B' = \varphi'(\xi)$. These profiles reveal that, in contrast to the standard Blasius flow, U_B' does not approach a constant as $\xi \to 0$.

When BM and TP are neglected (i.e. $Sc \to \infty$ and $Le \to \infty$), the concentration layer disappears with $\phi_B = \phi_\infty$ everywhere (see the vertical dotted lines in figure 3*e*). In this limit, the standard Blasius flow structure is recovered, with U_B' approaching a constant near the wall, as indicated by the dotted lines in figure 3(*b*).

Table 2 compares the base flow properties on the plate surface for varying ϕ_∞ and $T_w = 2$. The differences between the results obtained with and without BM and TP are negligible for $\phi_\infty < 10^{-3}$, but grow, due to the impact of the concentration layer, at larger ϕ_∞.

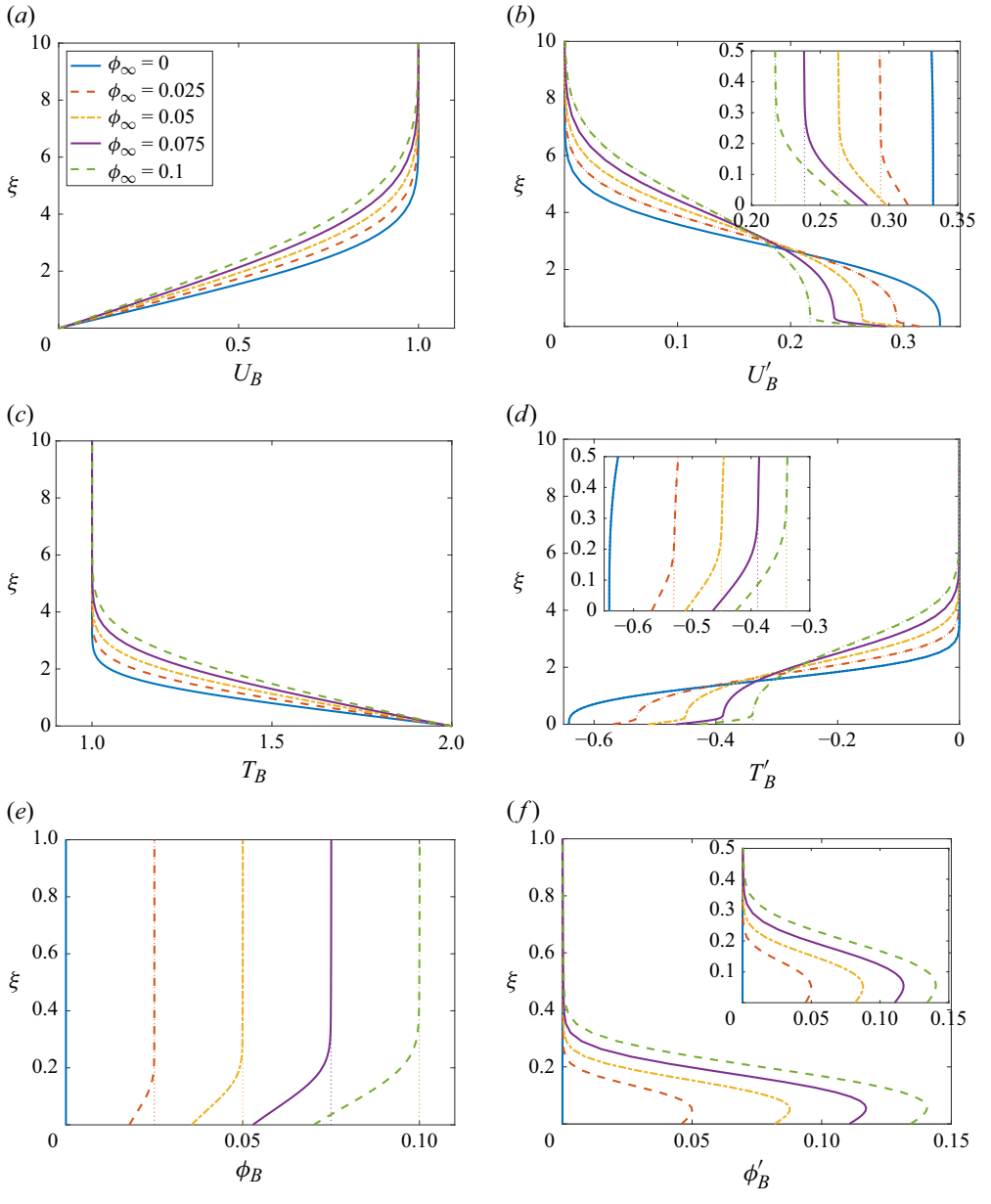

Figure 3. Steady base flow profiles for variable ϕ_∞ and $T_w = 2$, for Cu nanoparticles in water. (*a*) Streamwise velocity $U_B = f'(\xi)$, (*b*) $U_B' = f''(\xi)$, (*c*) temperature $T_B = \theta(\xi)$, (*d*) $T_B' = \theta'(\xi)$, (*e*) nanoparticle volume concentration $\phi_B = \varphi(\xi)$ and (*f*) $\phi_B' = \varphi'(\xi)$. Dotted lines depict the equivalent solutions in the instance $Le \to \infty$ and $Sc \to \infty$.

Since the base flow profiles in figure 3 are plotted against the density-weighted similarity variable ξ, a physically meaningful measure of the boundary-layer thickness is provided by the displacement thickness. The dimensional displacement thickness $\delta_1^* = x^*\delta_1/Re_x^{1/2}$ and momentum thickness $\delta_2^* = x^*\delta_2/Re_x^{1/2}$, for

$$\delta_1 = \int_0^\infty \frac{1}{\rho(\xi)} - \frac{f'(\xi)}{\rho_\infty}\,\mathrm{d}\xi \quad \text{and} \quad \delta_2 = \int_0^\infty \frac{f'(\xi)}{\rho_\infty}\left(1 - f'(\xi)\right)\,\mathrm{d}\xi, \qquad (3.10a,b)$$

ϕ_∞	$U_B'(0) = f''(0)$	$T_B'(0) = \theta'(0)$	$\phi_B(0) = \varphi(0)$
0	0.332057(0.332057)	−0.641309(−0.641309)	0.000000(0.000000)
10^{-6}	0.332057 (0.332056)	−0.641307 (−0.641304)	0.000001 (0.000001)
10^{-5}	0.332049 (0.332040)	−0.641276 (−0.641257)	0.000007 (0.000010)
10^{-4}	0.331979 (0.331884)	−0.640981 (−0.640790)	0.000073 (0.000100)
10^{-3}	0.331273 (0.330335)	−0.638043 (−0.636146)	0.000726 (0.001000)
10^{-2}	0.324446 (0.315631)	−0.610189 (−0.592849)	0.007229 (0.010000)
10^{-1}	0.271857 (0.217365)	−0.426271 (−0.339946)	0.070052 (0.100000)

Table 2. Base flow properties on $\xi = 0$ for variable ϕ_∞ and $T_w = 2$, where a prime denotes differentiation with respect to the similarity variable ξ. Solutions based on Cu nanoparticles in water, while the results in brackets correspond to the solutions obtained in the absence of BM and TP.

are shown in figure 4, along with the shape factor $H = \delta_1^*/\delta_2^*$. Here, $Re_x = U_\infty^* x^* \rho_{bf}^*/\mu_{bf}^*$ and $\rho_\infty = \rho_\infty^*/\rho_{bf}^*$ denotes the dimensionless free stream density. Results are plotted for all seven nanoparticle materials listed in table 1. For all but two of these materials, both δ_1 and δ_2 decrease as ϕ_∞ increases. The most significant reductions occur for Ag and Cu nanoparticles, which have the highest densities (and the largest non-dimensional $\hat{\rho}$ values). In contrast, silicon (Si) and aluminium (Al) nanoparticles, which have the lowest densities (and the smallest values of $\hat{\rho}$), show an increase in δ_1 and δ_2 as ϕ_∞ increases. (Solutions corresponding to the case without BM and TP are nearly identical to those shown in figure 4.)

The thermal displacement thickness $\delta_T^* = x^* \delta_T / Re_x^{1/2}$ and concentration displacement thickness $\delta_\phi^* = x^* \delta_\phi / Re_x^{1/2}$, for

$$\delta_T = \int_0^\infty \frac{1}{\rho(\xi)} - \frac{\theta(\xi) - T_w}{\rho_\infty (1 - T_w)} \, \mathrm{d}\xi \quad \text{and} \quad \delta_\phi = \int_0^\infty \frac{1}{\rho(\xi)} - \frac{\varphi(\xi)}{\rho_\infty \phi_\infty} \, \mathrm{d}\xi, \tag{3.11a,b}$$

are plotted in figure 5 as a function of ϕ_∞. In contrast to the displacement thickness δ_1, the thermal displacement thickness δ_T increases with increasing ϕ_∞ for all seven nanoparticle materials. The most pronounced increases are observed for the less dense materials, Al and Si. On the other hand, the concentration displacement thickness δ_ϕ (plotted on a semilogarithmic scale along the horizontal axis) exhibits only minor variations across the range of ϕ_∞ shown. However, noticeable differences arise between the materials. Notably, TiO_2 and Al_2O_3 exhibit larger values of δ_ϕ than the other materials. This can be attributed to their respective N_{BT} values being an order of magnitude smaller than those of the other materials (see table 1). Thus, TP effects are more dominant than BM effects for these particular materials. Moreover, as ϕ_∞ approaches zero, δ_ϕ tends towards a positive constant, indicating that φ approaches a limiting solution. This behaviour will be examined in further detail in § 3.4.

Despite the thickening of the thermal boundary-layer, the local Nusselt number, defined as

$$Nu = \frac{Re_x^{1/2} \rho_w k_w \theta'(0)}{1 - T_w}, \tag{3.12}$$

increases with increasing ϕ_∞, as shown in figure 6. Thus, all of the nanoparticles improve the heat transfer capabilities of the fluid. The most pronounced increases in Nu are observed for denser materials with higher thermal conductivities and smaller specific heat

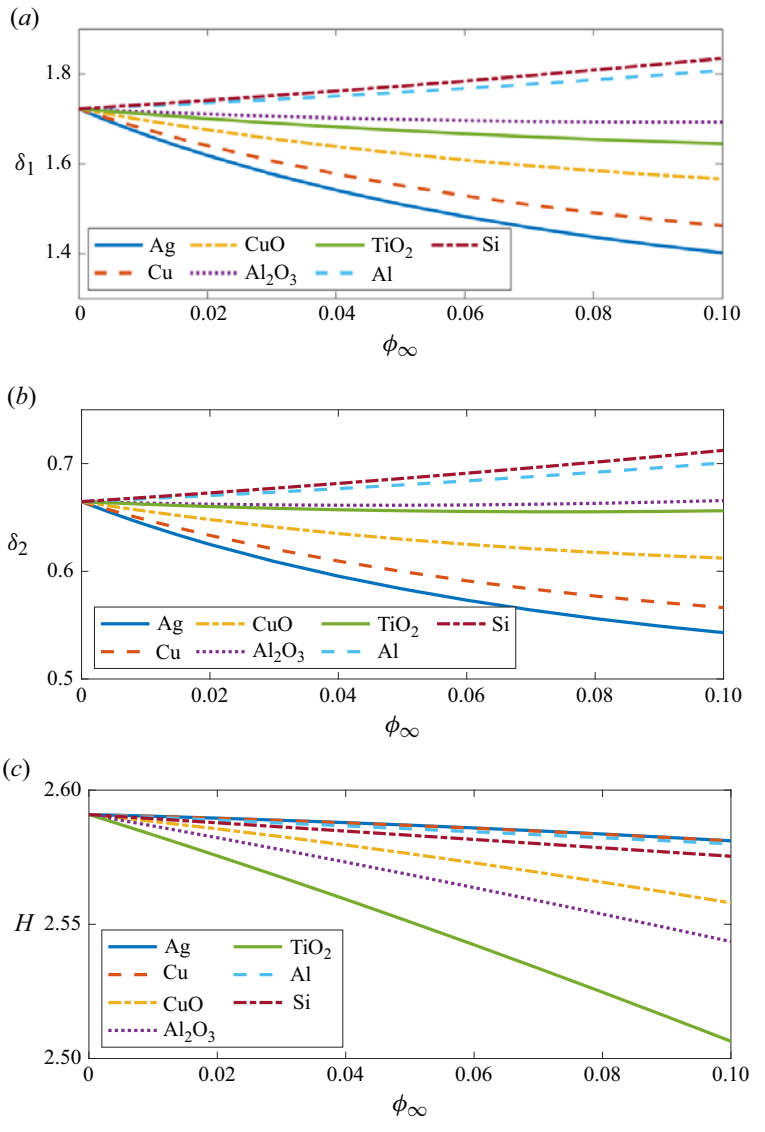

Figure 4. (*a*) Displacement thickness δ_1, (*b*) momentum thickness δ_2 and (*c*) shape factor H as functions of the free stream nanoparticle volume concentration ϕ_∞, for different nanoparticle materials.

capacities, such as Ag and Cu nanoparticles. Consequently, these materials have greater thermodynamic benefits.

3.4. *Asymptotic behaviour in the limit* $\phi_\infty \to 0$

The behaviour of the steady base flow is now examined in the limit as the free stream nanoparticle volume concentration ϕ_∞ approaches zero. Similarity variables f, θ and φ are expanded in powers of ϕ_∞, as

$$f(\xi) = f_0(\xi) + \phi_\infty f_1(\xi) + O(\phi_\infty^2), \tag{3.13a}$$

$$\theta(\xi) = \theta_0(\xi) + \phi_\infty \theta_1(\xi) + O(\phi_\infty^2), \tag{3.13b}$$

$$\varphi(\xi) = \phi_\infty \varphi_1(\xi) + O(\phi_\infty^2), \tag{3.13c}$$

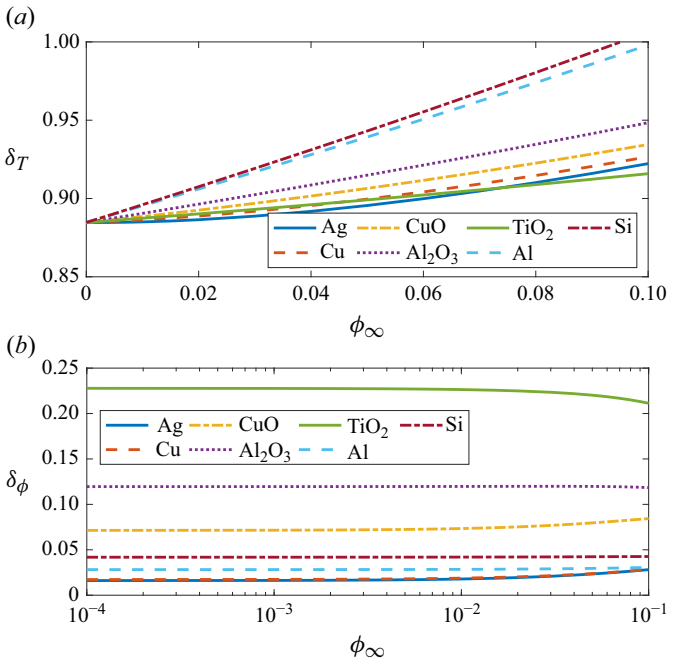

Figure 5. (*a*) Thermal displacement thickness δ_T and (*b*) concentration displacement thickness δ_ϕ as functions of the free stream nanoparticle volume concentration ϕ_∞, for different nanoparticle materials.

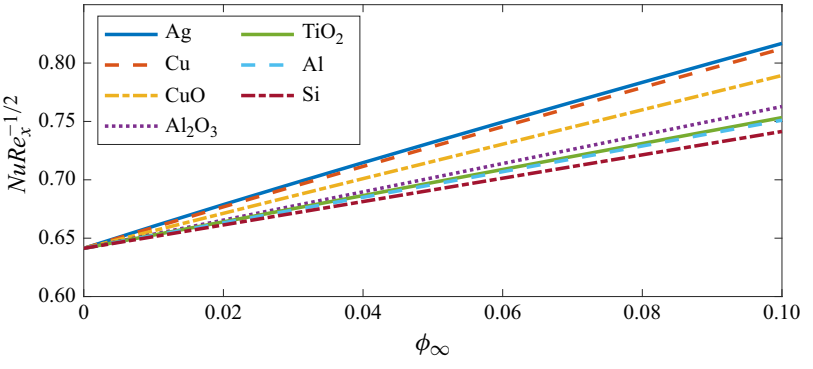

Figure 6. Scaled local Nusselt number $NuRe_x^{-1/2}$ as a function of the free stream nanoparticle volume concentration ϕ_∞, for different nanoparticle materials.

while the physical quantities μ, ρ, c and k are of the form

$$(\mu, \rho, c, k)(\xi) = 1 + \phi_\infty(\mu_1, \rho_1, c_1, k_1)(\xi) + O(\phi_\infty^2). \tag{3.13d}$$

Substituting (3.13) into (3.6*a*) and (3.6*b*) and retaining the leading-order terms yields the Blasius boundary-layer equations for the velocity and temperature

$$2f_0''' + f_0 f_0'' = 0 \quad \text{and} \quad 2\theta_0'' + Pr f_0 \theta_0' = 0, \tag{3.14a,b}$$

subject to the boundary conditions

$$f_0 = f_0' = 0, \quad \theta_0 = T_w \quad \text{on} \quad \xi = 0, \tag{3.14c-e}$$

$$f_0' \to 1, \quad \theta_0 \to 1 \quad \text{as} \quad \xi \to \infty. \tag{3.14f,g}$$

Moreover, substituting (3.13) into (3.6*c*) and equating terms of order ϕ_∞ gives the following second-order differential equation for φ_1:

$$\theta_0\varphi_1'' + \left(\theta_0' + \frac{\theta_0'}{N_{BT}\theta_0} + \frac{Scf_0}{2}\right)\varphi_1' + \frac{1}{N_{BT}}\left(\frac{\theta_0''}{\theta_0} - \left(\frac{\theta_0'}{\theta_0}\right)^2\right)\varphi_1 = 0, \tag{3.15a}$$

subject to the boundary conditions

$$\theta_0\varphi_1' + \frac{\varphi_1\theta_0'}{N_{BT}\theta_0} = 0 \quad \text{on} \quad \xi = 0, \tag{3.15b}$$

$$\varphi_1 \to 1 \quad \text{as} \quad \xi \to \infty. \tag{3.15c}$$

Substituting the solution of (3.14) into (3.15) establishes the limiting boundary-value problem for φ_1, with solutions presented in figure 7(*a*) for all seven nanoparticle materials given in table 1. These solutions illustrate the influence of the BM to TP ratio N_{BT} on the behaviour of the concentration layer. As N_{BT} decreases, the concentration layer becomes thicker. Notably, the solution corresponding to TiO_2, represented by the green solid line, exhibits an overshoot near the wall, where $\varphi_1 > 1$ before approaching the free stream value for larger ξ (beyond the range shown in figure 7*a*). Conversely, as N_{BT} increases and BM dominates diffusion effects, the nanoparticle volume concentration $\varphi_1 \to 1$ for all ξ, indicating a uniform concentration profile across the boundary layer.

Figures 7(*b*) and 7(*c*) compare the limiting solution φ_1 and numerical solutions ϕ_B/ϕ_∞ for $\phi_\infty \in [10^{-4}, 10^{-1}]$, for Cu and TiO_2 nanoparticles, respectively. In both cases, the numerical solution converges to the limiting profile φ_1 as $\phi_\infty \to 0$. Indeed, significant deviations only emerge for $\phi_\infty = 10^{-1}$.

3.5. *The concentration layer*

The base flow profiles in figures 3 and 7 reveal a thin concentration layer within the boundary layer, similar to the particle concentration layer reported by Pelekasis & Acrivos (1995) for the flow of a well-mixed particle suspension past a flat plate. As $Sc \to \infty$, the concentration layer narrows. Since $U_B \sim Y$ as $Y \to 0$, the following transformations are introduced to balance the diffusion and convection terms in (3.3*d*):

$$Y = Sc^{-1/3}\bar{Y}, \quad U_B = Sc^{-1/3}\bar{U}_B, \quad V_B = Sc^{-2/3}\bar{V}_B, \tag{3.16a–c}$$

which gives the rescaled concentration equation

$$\frac{\partial(\phi_B\bar{U}_B)}{\partial x} + \frac{\partial(\phi_B\bar{V}_B)}{\partial\bar{Y}} = \frac{\partial}{\partial\bar{Y}}\left(T_B\frac{\partial\phi_B}{\partial\bar{Y}} + \frac{\phi_B}{N_{BT}T_B}\frac{\partial T_B}{\partial\bar{Y}}\right). \tag{3.17}$$

Thus, the concentration layer has a characteristic thickness of $O(Re^{-1/2}Sc^{-1/3})$.

Substituting (3.16) into (3.3*a*)–(3.3*c*), with $Le \to \infty$ and

$$\phi_B = \phi_\infty + \frac{\psi(x,\bar{Y})}{Sc^{1/3}}, \tag{3.18}$$

gives to leading order,

$$\frac{\partial\bar{U}_B}{\partial x} + \frac{\partial\bar{V}_B}{\partial\bar{Y}} = 0, \quad \frac{\partial^2\bar{U}_B}{\partial\bar{Y}^2} = 0, \quad \frac{\partial^2 T_B}{\partial\bar{Y}^2} = 0. \tag{3.19a–c}$$

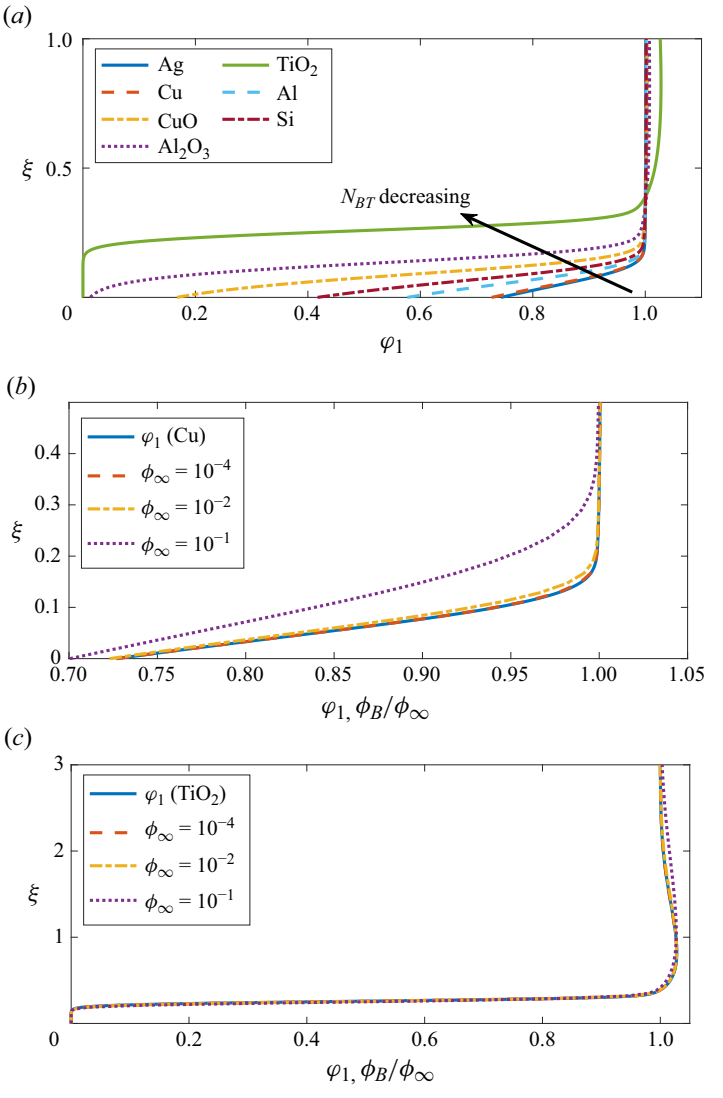

Figure 7. (*a*) Scaled profile of the nanoparticle volume concentration φ_1 in the limit $\phi_\infty \to 0$, for different nanoparticle materials. (*b,c*) Comparisons between the limiting solution φ_1 and numerical solutions ϕ_B/ϕ_∞ for $\phi_\infty = 10^{-4}$, $\phi_\infty = 10^{-2}$,and $\phi_\infty = 10^{-1}$, for Cu and TiO_2 nanoparticles.

The leading-order term in the concentration equation (3.17) is also given by (3.19*a*). Thus,

$$\bar{U}_B = \frac{\hat{\lambda}\bar{Y}}{x^{1/2}}, \quad \bar{V}_B = \frac{\hat{\lambda}\bar{Y}^2}{4x^{3/2}}, \quad T_B = T_w + \frac{\hat{\sigma}\,\bar{Y}}{Sc^{1/3}x^{1/2}}, \tag{3.20a–c}$$

for $\hat{\lambda} = \rho_w f''(0)$ and $\hat{\sigma} = \rho_w \theta'(0)$.

The next order term in the concentration equation (3.17) is given as

$$\bar{U}_B \frac{\partial \psi}{\partial x} + \bar{V}_B \frac{\partial \psi}{\partial \bar{Y}} = T_w \frac{\partial^2 \psi}{\partial \bar{Y}^2}, \tag{3.21a}$$

with boundary conditions

$$\frac{\partial \psi}{\partial \bar{Y}} + \frac{\phi_\infty \hat{\sigma}}{N_{BT} T_w^2 x^{1/2}} = 0 \quad \text{on} \quad \bar{Y} = 0 \tag{3.21b}$$

and

$$\psi \to 0 \quad \text{as} \quad \bar{Y} \to \infty. \tag{3.21c}$$

Introducing the similarity transformation

$$\psi(x, \bar{Y}) = \frac{\phi_\infty \hat{\sigma} \Psi(\bar{\eta})}{N_{BT} \hat{\lambda}^{1/3} T_w^{5/3}}, \tag{3.22a}$$

for

$$\bar{\eta} = \left(\frac{\hat{\lambda}}{T_w}\right)^{1/3} \frac{\bar{Y}}{x^{1/2}}, \tag{3.22b}$$

gives the similarity equation

$$\frac{d^2\Psi}{\mathrm{d}\bar{\eta}^2} + \frac{\bar{\eta}^2}{4} \frac{\mathrm{d}\Psi}{\mathrm{d}\bar{\eta}} = 0, \tag{3.23a}$$

with boundary conditions

$$\frac{\mathrm{d}\Psi}{\mathrm{d}\bar{\eta}} = -1 \quad \text{on} \quad \bar{\eta} = 0 \tag{3.23b}$$

and

$$\Psi \to 0 \quad \text{as} \quad \bar{\eta} \to \infty. \tag{3.23c}$$

The solution for Ψ is given in terms of the upper incomplete Gamma function Γ,

$$\Psi(\bar{\eta}) = \left(\frac{2}{3}\right)^{2/3} \Gamma\left(\frac{1}{3}, \frac{\bar{\eta}^3}{12}\right), \tag{3.24}$$

and is plotted in figure 8(*a*). At the wall, $\Psi(0) \approx 2.0444$. Hence, to a first approximation, the nanoparticle volume concentration is given by

$$\phi_B = \phi_\infty \left(1 + \frac{\hat{\sigma} \Psi(\bar{\eta})}{N_{BT} \hat{\lambda}^{1/3} T_w^{5/3} Sc^{1/3}}\right). \tag{3.25}$$

Figures 8(*b*) and 8(*c*) compare the exact nanoparticle volume concentration profiles ϕ_B, obtained by solving (3.6), with the approximate solution given by (3.25), for Cu nanoparticles and $T_w = 2$. Results are plotted for $\phi_\infty = 10^{-3}$ and $\phi_\infty = 10^{-2}$. In both cases, the approximate solution is qualitatively similar to the exact solution, with only minor differences near the wall, corresponding to a maximum relative error of approximately 3 %. Such small differences are to be expected since $N_{BT} Sc^{1/3} \sim O(1)$ for the parameter settings used in figures 8(*b*) and 8(*c*). For materials with smaller N_{BT} values, such as Al_2O_3 and TiO_2, the approximation is less accurate, and higher-order terms are required to improve the solution. However, by increasing both Sc and N_{BT}, as is modelled in figures 8(*d*) and 8(*e*), the agreement between the exact and approximate solutions improves significantly, with the maximum relative error reduced to 0.001 %.

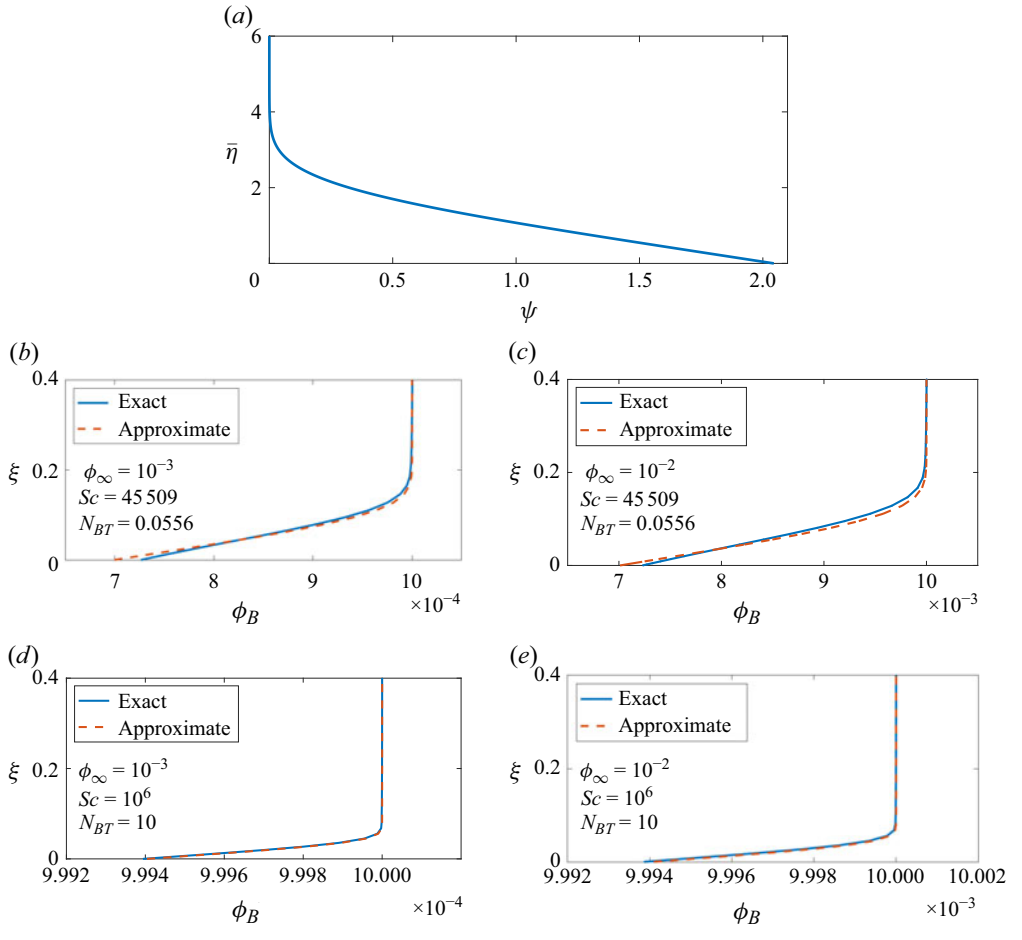

Figure 8. (*a*) Similarity solution Ψ for the nanoparticle volume concentration, as given by (3.24). (*b–e*) Nanoparticle volume concentration profiles ϕ_B given by the exact solution to (3.6) (solid blue lines) and the approximate solution (3.25) (dashed red), for Cu nanoparticles.

4. Linear stability analysis

4.1. *Linearised stability equations*

The linear stability equations are derived by decomposing the total velocity, pressure, temperature and nanoparticle volume concentration fields as

$$u = U_B + \epsilon\tilde{u}, \quad v = Re^{-1/2}V_B + \epsilon\tilde{v}, \quad w = \epsilon\tilde{w},$$
$$p = \epsilon\tilde{p}, \quad T = T_B + \epsilon\tilde{T}, \quad \phi = \phi_B + \epsilon\tilde{\phi}, \tag{4.1a–f}$$

for perturbations $\tilde{\boldsymbol{q}} = (\tilde{\boldsymbol{u}}, \tilde{p}, \tilde{T}, \tilde{\phi})$, with $\tilde{\boldsymbol{u}} = (\tilde{u}, \tilde{v}, \tilde{w})$ and $\epsilon \ll 1$. Similarly,

$$\rho = \rho_B + \epsilon\tilde{\rho}, \quad \rho c = (\rho c)_B + \epsilon\tilde{\rho}\tilde{c}, \quad c = c_B + \epsilon\tilde{c},$$
$$\mu = \mu_B + \epsilon\tilde{\mu}, \quad k = k_B + \epsilon\tilde{k}. \tag{4.2a–e}$$

Here, base flow quantities $\boldsymbol{Q}_B = (U_B, V_B, T_B, \phi_B)$ depend on x and y, while perturbations $\tilde{\boldsymbol{q}}$ are functions of $\boldsymbol{x}$ and t. Substituting (4.1) and (4.2) into (2.12), and linearising in ϵ,

gives the following linear stability equations:

$$\rho_B \boldsymbol{\nabla}\cdot\tilde{\boldsymbol{u}} + \frac{\partial\tilde{\rho}}{\partial t} + U_B\frac{\partial\tilde{\rho}}{\partial x} + \rho_{B,y}\tilde{v} = g_1(V_B,\,\boldsymbol{Q}_{B,x}), \tag{4.3a}$$

$$\rho_B\left(\frac{\partial\tilde{u}}{\partial t} + U_B\frac{\partial\tilde{u}}{\partial x} + U_{B,y}\tilde{v}\right) = -\frac{\partial\tilde{p}}{\partial x} + \frac{1}{Re}\left(\mu_B\left(\nabla^2\tilde{u} + \frac{1}{3}\frac{\partial}{\partial x}\boldsymbol{\nabla}\cdot\tilde{\boldsymbol{u}}\right)\right.$$
$$\left. + \mu_{B,y}\left(\frac{\partial\tilde{v}}{\partial x} + \frac{\partial\tilde{u}}{\partial y}\right) + U_{B,yy}\tilde{\mu} + U_{B,y}\frac{\partial\tilde{\mu}}{\partial y}\right) + g_2(V_B,\,\boldsymbol{Q}_{B,x}), \tag{4.3b}$$

$$\rho_B\left(\frac{\partial\tilde{v}}{\partial t} + U_B\frac{\partial\tilde{v}}{\partial x}\right) = -\frac{\partial\tilde{p}}{\partial y} + \frac{1}{Re}\left(\mu_B\left(\nabla^2\tilde{v} + \frac{1}{3}\frac{\partial}{\partial y}\boldsymbol{\nabla}\cdot\tilde{\boldsymbol{u}}\right)\right.$$
$$\left. + \frac{2\mu_{B,y}}{3}\left(2\frac{\partial\tilde{v}}{\partial y} - \left(\frac{\partial\tilde{u}}{\partial x} + \frac{\partial\tilde{w}}{\partial z}\right)\right) + U_{B,y}\frac{\partial\tilde{\mu}}{\partial x}\right) + g_3(V_B,\,\boldsymbol{Q}_{B,x}), \tag{4.3c}$$

$$\rho_B\left(\frac{\partial\tilde{w}}{\partial t} + U_B\frac{\partial\tilde{w}}{\partial x}\right) = -\frac{\partial\tilde{p}}{\partial z} + \frac{1}{Re}\left(\mu_B\left(\nabla^2\tilde{w} + \frac{1}{3}\frac{\partial}{\partial z}\boldsymbol{\nabla}\cdot\tilde{\boldsymbol{u}}\right)\right.$$
$$\left. + \mu_{B,y}\left(\frac{\partial\tilde{v}}{\partial z} + \frac{\partial\tilde{w}}{\partial y}\right)\right) + g_4(V_B,\,\boldsymbol{Q}_{B,x}), \tag{4.3d}$$

$$\rho_B T_B\left(\frac{\partial\tilde{c}}{\partial t} + U_B\frac{\partial\tilde{c}}{\partial x} + c_{B,y}\tilde{v}\right) + (\rho c)_B\left(\frac{\partial\tilde{T}}{\partial t} + U_B\frac{\partial\tilde{T}}{\partial x} + T_{B,y}\tilde{v}\right)$$
$$= \frac{1}{RePr}\left(\frac{\partial}{\partial y}\left(k_B\frac{\partial\tilde{T}}{\partial y} + T_{B,y}\tilde{k}\right) + k_B\widehat{\nabla}^2\tilde{T}\right)$$
$$+ \frac{1}{RePrLe}\left(T_{B,y}\mathcal{A} + \mathcal{B}\frac{\partial\tilde{T}}{\partial y}\right) + g_5(V_B,\,\boldsymbol{Q}_{B,x}), \tag{4.3e}$$

$$\phi_B\boldsymbol{\nabla}\cdot\tilde{\boldsymbol{u}} + \frac{\partial\tilde{\phi}}{\partial t} + U_B\frac{\partial\tilde{\phi}}{\partial x} + \phi_{B,y}\tilde{v} = \frac{1}{ReSc}\left(\frac{\partial\mathcal{A}}{\partial y} + T_B\widehat{\nabla}^2\tilde{\phi} + \frac{\phi_B}{N_{BT}T_B}\hat{\nabla}^2\tilde{T}\right)$$
$$+ g_6(V_B,\,\boldsymbol{Q}_{B,x}), \tag{4.3f}$$

where functions $g_\star$ depend on the wall-normal velocity V_B and x-derivatives of the base flow $\boldsymbol{Q}_B$, and

$$\mathcal{A} = T_B\frac{\partial\tilde{\phi}}{\partial y} + \phi_{B,y}\tilde{T} + \frac{1}{N_{BT}T_B}\left(\phi_B\frac{\partial\tilde{T}}{\partial y} + T_{B,y}\tilde{\phi} - \frac{\phi_B T_{B,y}}{T_B}\tilde{T}\right), \tag{4.4}$$

$$\mathcal{B} = \phi_{B,y}T_B + \frac{\phi_B T_{B,y}}{N_{BT}T_B} \tag{4.5}$$

and

$$\widehat{\nabla}^2 = \frac{\partial^2}{\partial x^2} + \frac{\partial^2}{\partial z^2}. \tag{4.6}$$

(The exact form of the functions $g_\star$ are given in Appendix B.) The corresponding boundary conditions are given as

$$\tilde{u} = \tilde{v} = \tilde{w} = \tilde{T} = \mathcal{A} = 0 \quad \text{on} \quad y = 0, \tag{4.7a–e}$$

and

$$\tilde{u} \to 0,\ \tilde{v} \to 0,\ \tilde{w} \to 0,\ \tilde{p} \to 0,\ \tilde{T} \to 0,\ \tilde{\phi} \to 0 \quad \text{as} \quad y \to \infty. \tag{4.7f–k}$$

The length scale L^* used in the subsequent linear stability analysis is based on the displacement thickness δ_1^*, to give the Reynolds number

$$R = \frac{U_\infty^* \delta_1^* \rho_{bf}^*}{\mu_{bf}^*}, \tag{4.8}$$

which ensures consistency with earlier investigations (Mack 1984; Schmid & Henningson 2001). This gives the following relationships: $R = \delta_1 Re_x^{1/2}$ and $R = \delta_1 (xRe)^{1/2}$. Consequently, Re in the system of equations (4.3) is replaced with R.

Additionally, the parallel flow approximation is imposed, where the flow is assumed to be in the x-direction and depends only on the wall-normal y-direction, i.e. $g_\star = 0$. Subsequently, perturbations $\tilde{\boldsymbol{q}}$ are decomposed into the normal mode form

$$\tilde{\boldsymbol{q}}(\boldsymbol{x}, t) = \breve{\boldsymbol{q}}(y) \exp\left(\mathrm{i}(\alpha x + \beta z - \omega t)\right) + \text{c.c.}, \tag{4.9}$$

(and similarly for quantities $\tilde{\rho}$, $\tilde{\mu}$, etc.) for a streamwise wavenumber $\alpha \in \mathbb{R}$, spanwise wavenumber $\beta \in \mathbb{R}$, and frequency $\omega \in \mathbb{C}$. Here, c.c. denotes the complex conjugate. Consequently, (4.3) become

$$\rho_B \left(\mathrm{i}\left(\alpha \breve{u} + \beta \breve{w}\right) + \mathrm{D}\breve{v}\right) + \mathrm{i}\left(\alpha U_B - \omega\right) \breve{\rho} + \rho_{B,y} \breve{v} = 0, \tag{4.10a}$$

$$\begin{aligned}\rho_B \left(\mathrm{i}\left(\alpha U_B - \omega\right) \breve{u} + U_{B,y} \breve{v}\right) = -\mathrm{i}\alpha \breve{p} + \frac{1}{R}\Bigg(\mu_B\Bigg(\left(\mathrm{D}^2 - \left(\alpha^2 + \beta^2\right)\right)\breve{u} \\ + \frac{\mathrm{i}\alpha}{3}\left(\mathrm{i}\left(\alpha \breve{u} + \beta \breve{w}\right) + \mathrm{D}\breve{v}\right)\Bigg) + \mu_{B,y}\left(\mathrm{i}\alpha \breve{v} + \mathrm{D}\breve{u}\right) + \left(U_{B,yy} + U_{B,y}\mathrm{D}\right)\breve{\mu}\Bigg),\end{aligned} \tag{4.10b}$$

$$\begin{aligned}\mathrm{i}\rho_B \left(\alpha U_B - \omega\right) \breve{v} = -\mathrm{D}\breve{p} + \frac{1}{R}\Bigg(\mu_B\Bigg(\left(\mathrm{D}^2 - \left(\alpha^2 + \beta^2\right)\right)\breve{v} + \frac{\mathrm{D}}{3}\left(\mathrm{i}\left(\alpha \breve{u} + \beta \breve{w}\right) + \mathrm{D}\breve{v}\right)\Bigg) \\ + \frac{2\mu_{B,y}}{3}\left(2\mathrm{D}\breve{v} - \mathrm{i}\left(\alpha \breve{u} + \beta \breve{w}\right)\right) + \mathrm{i}\alpha U_{B,y}\breve{\mu}\Bigg),\end{aligned} \tag{4.10c}$$

$$\begin{aligned}\mathrm{i}\rho_B \left(\alpha U_B - \omega\right) \breve{w} = -\mathrm{i}\beta \breve{p} + \frac{1}{R}\Bigg(\mu_B\Bigg(\left(\mathrm{D}^2 - \left(\alpha^2 + \beta^2\right)\right)\breve{w} \\ + \frac{\mathrm{i}\beta}{3}\left(\mathrm{i}\left(\alpha \breve{u} + \beta \breve{w}\right) + \mathrm{D}\breve{v}\right)\Bigg) + \mu_{B,y}\left(\mathrm{i}\beta \breve{v} + \mathrm{D}\breve{w}\right)\Bigg),\end{aligned} \tag{4.10d}$$

$$\begin{aligned}\rho_B T_B \left(\mathrm{i}\left(\alpha U_B - \omega\right) \breve{c} + c_{B,y} \breve{v}\right) + (\rho c)_B \left(\mathrm{i}\left(\alpha U_B - \omega\right) \breve{T} + T_{B,y} \breve{v}\right) \\ = \frac{1}{RPr}\left(\mathrm{D}\left(k_B \mathrm{D}\breve{T} + T_{B,y}\breve{k}\right) - \left(\alpha^2 + \beta^2\right) k_B \breve{T}\right) + \frac{1}{RPrLe}\left(T_{B,y}\mathcal{A} + \mathcal{B}\mathrm{D}\breve{T}\right),\end{aligned} \tag{4.10e}$$

$$\begin{aligned}\phi_B \left(\mathrm{i}\left(\alpha \breve{u} + \beta \breve{w}\right) + \mathrm{D}\breve{v}\right) + \mathrm{i}\left(\alpha U_B - \omega\right) \breve{\phi} + \phi_{B,y} \breve{v} \\ = \frac{1}{RSc}\left(\mathrm{D}\mathcal{A} - \left(\alpha^2 + \beta^2\right)\left(T_B \breve{\phi} + \frac{\phi_B}{N_{BT} T_B}\breve{T}\right)\right),\end{aligned} \tag{4.10f}$$

where $\mathrm{D} = d/\mathrm{d}y$. The exact form of the perturbed quantities, including $\breve{\rho}$, $\breve{\mu}$, etc., are given in Appendix B.

N	l	$\omega\ (\phi_\infty = 10^{-4})$	$\omega\ (\phi_\infty = 10^{-2})$	$\omega\ (\phi_\infty = 10^{-1})$
32	2	$0.11931 - \mathrm{i}0.00035$	$0.11987 - \mathrm{i}0.00019$	$0.11141 + \mathrm{i}0.00308$
64	2	$0.11928 - \mathrm{i}0.00029$	$0.11844 + \mathrm{i}0.00008$	$0.11384 + \mathrm{i}0.00151$
96	2	$0.11929 - \mathrm{i}0.00028$	$0.11845 + \mathrm{i}0.00009$	$0.11382 + \mathrm{i}0.00153$
128	2	$0.11929 - \mathrm{i}0.00028$	$0.11845 + \mathrm{i}0.00009$	$0.11382 + \mathrm{i}0.00153$
32	3	$0.11926 - \mathrm{i}0.00036$	$0.12153 - \mathrm{i}0.00029$	$0.11162 + \mathrm{i}0.00313$
64	3	$0.11928 - \mathrm{i}0.00029$	$0.11845 + \mathrm{i}0.00008$	$0.11384 + \mathrm{i}0.00151$
96	3	$0.11929 - \mathrm{i}0.00028$	$0.11845 + \mathrm{i}0.00009$	$0.11383 + \mathrm{i}0.00152$
128	3	$0.11929 - \mathrm{i}0.00028$	$0.11845 + \mathrm{i}0.00009$	$0.11383 + \mathrm{i}0.00151$
32	4	$0.11925 - \mathrm{i}0.00033$	$0.11823 + \mathrm{i}0.00088$	$0.11229 - \mathrm{i}0.00199$
64	4	$0.11928 - \mathrm{i}0.00029$	$0.11844 + \mathrm{i}0.00008$	$0.11382 + \mathrm{i}0.00153$
96	4	$0.11929 - \mathrm{i}0.00028$	$0.11844 + \mathrm{i}0.00008$	$0.11383 + \mathrm{i}0.00152$
128	4	$0.11929 - \mathrm{i}0.00028$	$0.11845 + \mathrm{i}0.00009$	$0.11383 + \mathrm{i}0.00152$

Table 3. Frequencies $\omega = \omega_r + \mathrm{i}\omega_i$ for variable N and l, for $R = 500$, $\alpha = 0.3$, $\beta = 0$, $T_w = 2$ and $\phi_\infty = 10^{-4}$, $\phi_\infty = 10^{-2}$, $\phi_\infty = 10^{-1}$. Here, $\omega_i > 0$ corresponds to linearly unstable behaviour.

4.2. *Numerical methods*

A temporal linear stability analysis was conducted using the Chebyshev collocation method developed by Trefethen (2000). Derivatives in the y-direction were approximated using Chebyshev matrices, with N Chebyshev mesh points mapped from the semi-infinite physical domain $y \in [0, \infty)$ onto the computational interval $\zeta \in [1, -1]$ via the coordinate transformation

$$y = \frac{l(1-\zeta)}{1+\zeta}, \tag{4.11}$$

where l is a stretching parameter.

The linear stability equations (4.10) were transformed into the following eigenvalue problem:

$$\boldsymbol{A}\breve{\boldsymbol{q}}^T = \omega \boldsymbol{B}\breve{\boldsymbol{q}}^T, \tag{4.12}$$

where $\boldsymbol{A}$ and $\boldsymbol{B}$ are $6N \times 6N$ matrices. The frequencies ω and the corresponding linear perturbations $\breve{\boldsymbol{q}}$ were then computed using the `eig` command in MATLAB.

Table 3 presents the frequency ω corresponding to the TS wave for varying values of N and l, for Cu nanoparticles and free stream nanoparticle volume concentrations $\phi_\infty \in [10^{-4}, 10^{-1}]$. In each case, the Reynolds number $R = 500$, the streamwise wavenumber $\alpha = 0.3$, the spanwise wavenumber $\beta = 0$ and the wall temperature $T_w = 2$. The results are identical to four decimal places for all l considered when $N \geqslant 64$, indicating that the thin concentration layer is well-resolved and the frequencies ω have converged. Therefore, for the remainder of this investigation, $N = 96$ Chebyshev mesh points were used with the mapping parameter $l = 2$.

4.3. *Numerical results*

In the following linear stability analysis, unless stated otherwise, the nanofluid is composed of Cu nanoparticles dispersed in a base fluid of water. In addition, the wall temperature $T_w = 2$. (The case $T_w = 2$ was selected as a representative case. However, as shown in Appendix C, variations in wall temperature have negligible influence on the results.)

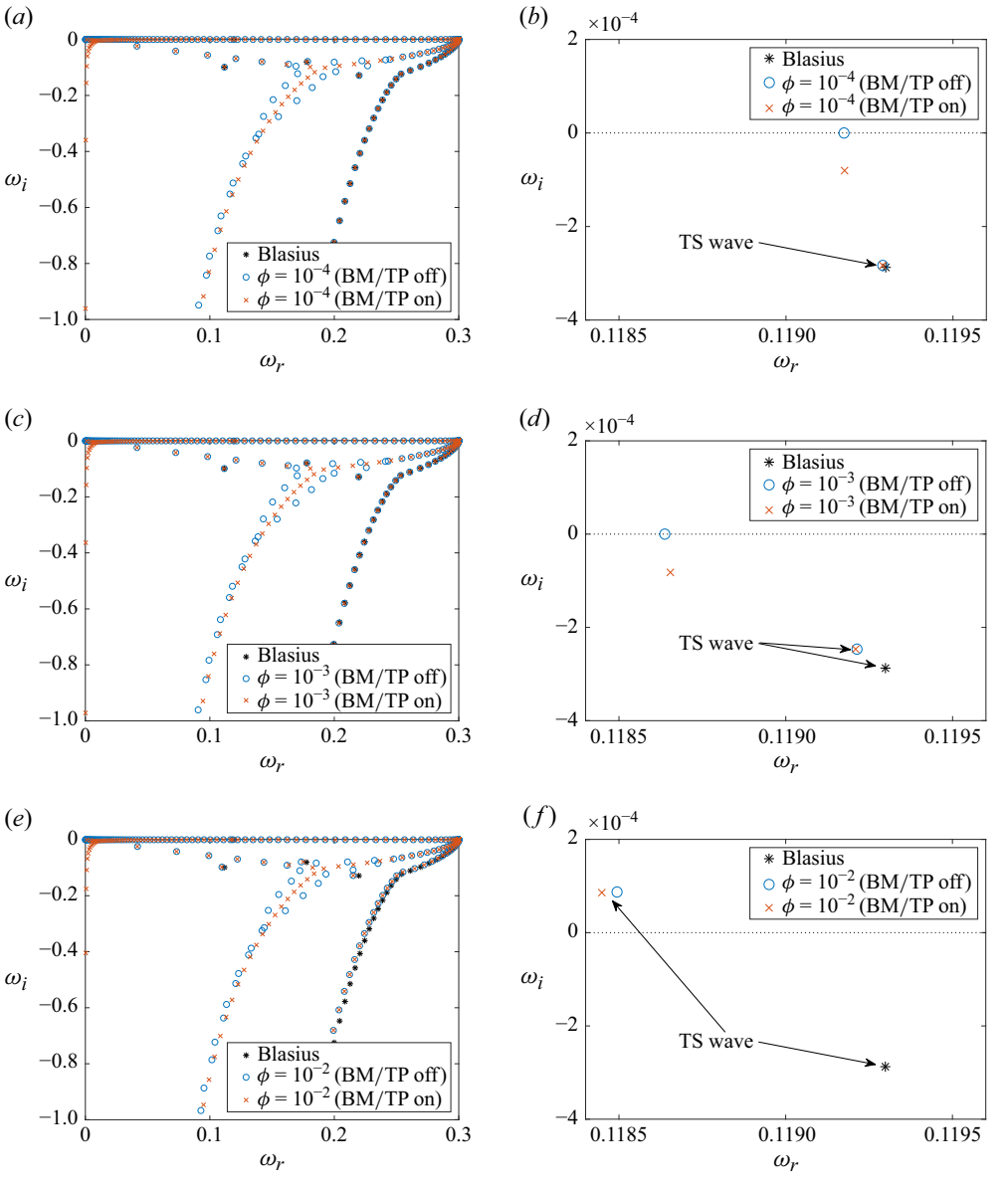

Figure 9. Eigenspectrum in the (ω_r, ω_i)-plane for $R = 500$, $\alpha = 0.3$, $\beta = 0$, $T_w = 2$, and (a,b) $\phi_\infty = 10^{-4}$, (c,d) $\phi_\infty = 10^{-3}$ and (e,f) $\phi_\infty = 10^{-2}$. Black asterisk markers represent solutions of the Blasius flow, while blue circles and red crosses represent solutions of the nanofluid flow without (BM/TP off) and with (BM/TP on) BM and TP.

4.3.1. *Eigenspectrum*

Figure 9 presents a representative eigenspectrum in the complex ω-plane for the parameter settings $R = 500$, $\alpha = 0.3$ and $\beta = 0$, and three values of ϕ_∞. For the standard Blasius flow without nanoparticles, these conditions are linearly stable. The left-hand plots display the eigenspectrum on a large scale, while the right-hand plots provide a zoomed-in view. The blue circular markers correspond to solutions where BM and TP are ignored, whereas

the red crosses indicate the corresponding solutions when these effects are included. The black star markers represent the eigenspectrum for the Blasius flow without nanoparticles, where the nanoparticle volume concentration equations have been removed from the analysis.

Consistent with previous studies (Mack 1976; Grosch & Salwen 1978; Salwen & Grosch 1981; Schmid & Henningson 2001), the eigenspectrum consists of multiple branches. A discrete set of modes are located on the A-branch (Mack 1976) in the upper left-hand corner of figure 9(*a,c,e*). This branch contains the TS wave, which is highlighted in the right-hand plots and discussed further below. Additionally, the eigenspectrum features three continuous branches, each associated with different governing equations. (The eigenspectrum shown is a discrete representation of the continuous spectrum, with the resolution governed by the number of Chebyshev mesh points N.) The first two branches, approximately aligned with the vertical axis, are associated with the momentum and energy equations, respectively. As the number of Chebyshev mesh points N increases, these two branches shift to the right towards the vertical line $\omega_r \to \alpha$, although their qualitative behaviour is unchanged. The third continuous branch, associated with the nanoparticle volume concentration equation, runs parallel to the real ω-line but with a negative imaginary part. Like the other two continuous branches, this branch also shifts to the right as N increases, but at a significantly slower rate due to the size of the Schmidt number Sc. Notably, when BM and TP are neglected, this branch is located along the real ω-line (i.e. $\omega_i = 0$), as expected, since equation (4.10*f*) simplifies to

$$(\alpha U_B - \omega)\,\breve{\phi} = 0 \tag{4.13}$$

in this case.

The zoomed-in plots on the right-hand side of figure 9 focus on the behaviour of the frequency ω of the TS wave as the free stream nanoparticle volume concentration ϕ_∞ increases. For $\phi_\infty = 10^{-4}$, the value of ω closely matches that of the Blasius flow without nanoparticles, with linearly stable conditions, as the imaginary part of ω is negative. However, as ϕ_∞ increases, a noticeable shift occurs. At $\phi_\infty = 10^{-3}$, the frequency ω shifts slightly to the left and upward in the ω-plane, remaining linearly stable but less stable than the standard Blasius flow. With a further increase to $\phi_\infty = 10^{-2}$, ω moves into the upper half-plane, where a positive imaginary part indicates linearly unstable behaviour. Thus, for the given flow conditions, the nanofluid destabilises the TS wave. Furthermore, the differences in ω obtained with and without the effects of BM and TP are minimal, with only slight variations in the real component and no discernible changes in the imaginary component. (In addition to the frequency ω of the TS wave, eigenspectra from the branch arising from the nanoparticle volume concentration equation are also shown in figure 9(*b,d*), further illustrating how this branch aligns with the real ω-axis.)

Figure 10 further illustrates the variation of the frequency ω of the TS wave as the free stream nanoparticle volume concentration ϕ_∞ increases, for the same conditions as given in figure 9. The plots show the evolution of both the real and imaginary components of ω with increasing ϕ_∞, supporting the trend observed in figure 9. As more nanoparticles are added to the base fluid, the TS wave becomes increasingly destabilised, with the imaginary part of ω shifting from negative to positive values near $\phi_\infty = 0.008$, signalling the onset of linear instability. Additionally, solutions demonstrate that the effects of BM and TP are negligible, since the differences between cases without (solid blue lines) and with (dashed red) these effects are minimal, with only slight variations in the real part of ω and no significant impact on the imaginary part.

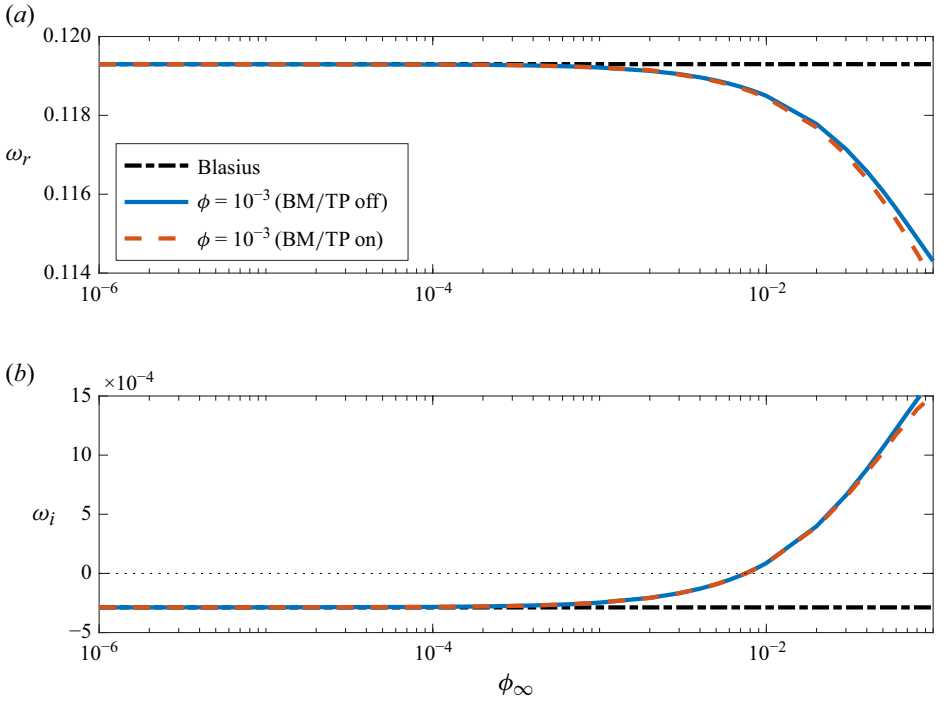

Figure 10. Frequency $\omega = \omega_r + \mathrm{i}\omega_i$ as a function of ϕ_∞ for $R = 500$, $\alpha = 0.3$, $\beta = 0$ and $T_w = 2$. (*a*) Real part and (*b*) imaginary part. The solid blue and dashed red lines represent solutions of the nanofluid flow without (BM/TP off) and with (BM/TP on) BM and TP. The horizontal chain lines indicate the corresponding solutions for the Blasius flow without nanoparticles.

4.3.2. *Three-dimensional instabilities*

Although Squire's theorem cannot be applied directly to the full linear stability equations (4.10), it is applicable to the simplified linear stability equations that neglect BM and TP. Since these diffusion effects have a minimal impact on both the base flow and the linear stability calculations, we conclude that Squire's theorem is approximately valid for the full equations. Consequently, it is sufficient to limit the stability analysis to two-dimensional instabilities.

This conclusion is supported by the results shown in figure 11, which plots the temporal growth rate ω_i as a function of the streamwise wavenumber α, for the Reynolds number $R = 600$, spanwise wavenumbers $\beta \in [0, 0.1]$ and nanoparticle volume concentrations $\phi_\infty \in [10^{-4}, 10^{-2}]$. The results indicate that ω_i decreases as β increases, confirming that two-dimensional instabilities are more unstable than three-dimensional instabilities. Therefore, based on this and further observations, the remainder of this study focuses on two-dimensional disturbances by setting $\beta = 0$.

4.3.3. *Conditions for neutral stability*

The neutral conditions (ω, R) for linear instability were computed using streamwise wavenumber increments of $\Delta\alpha = 10^{-4}$. To accurately trace the frequency ω associated with the TS wave within the complex ω-plane, small Reynolds number steps $\Delta R = 0.01$ were used. This ensured that the TS frequency was correctly identified, minimising interference with the eigenspectra found on the branch due to the nanoparticle volume concentration equation. The critical Reynolds number for the Blasius flow, in the absence

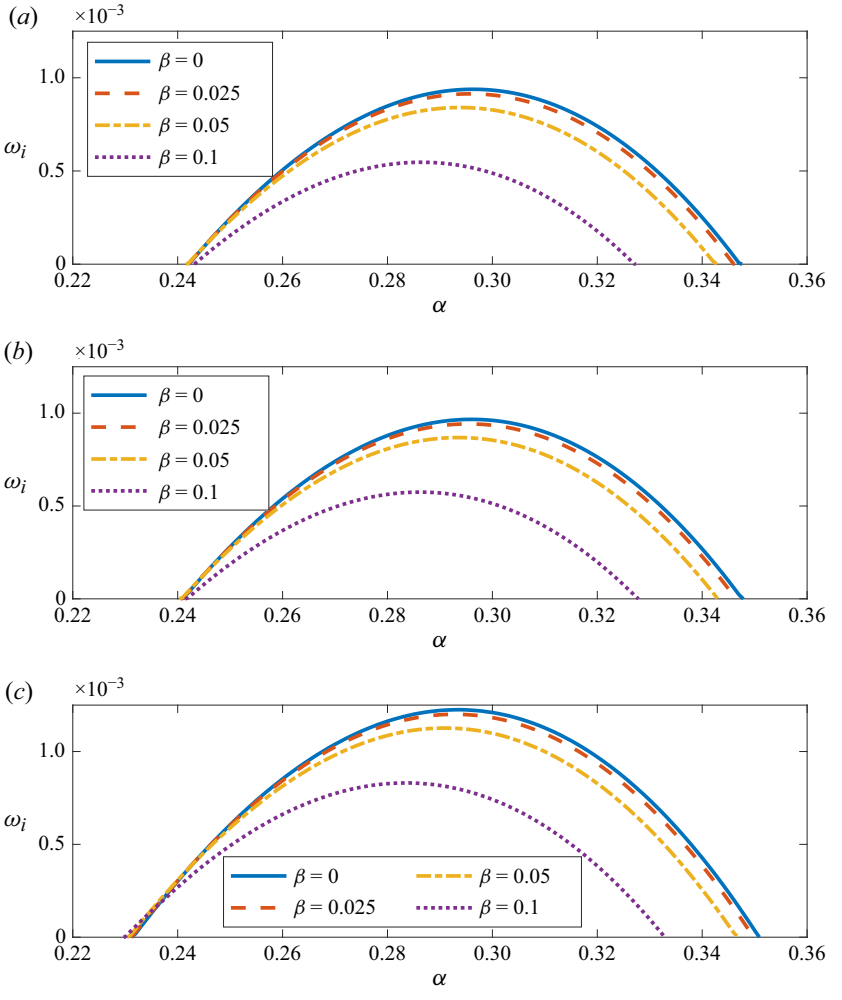

Figure 11. Temporal growth rate ω_i as a function of the streamwise wavenumber α for $R = 600$, $T_w = 2$, $\beta \in [0, 0.1]$ and (*a*) $\phi_\infty = 10^{-4}$, (*b*) $\phi_\infty = 10^{-3}$ and (*c*) $\phi_\infty = 10^{-2}$.

of nanoparticles, was obtained as $R_c \approx 519.4$ for a streamwise wavenumber $\alpha_c \approx 0.304$, frequency $\omega_c \approx 0.121$ and phase speed $s_c = \omega_c/\alpha_c \approx 0.397$, in agreement with previous studies (Schmid & Henningson 2001).

Neutral stability curves were obtained for free stream nanoparticle volume concentrations $\phi_\infty \in [0, 4 \times 10^{-2}]$, with solutions for the Cu nanoparticles shown in figure 12(*a*). The destabilisation of the TS wave is further demonstrated, with neutral stability curves shifting horizontally to the left and smaller Reynolds numbers as ϕ_∞ increases. Notably, there is no discernible vertical variation in the neutral stability curves. Thus, while the critical Reynolds number R_c shrinks, the corresponding frequency ω_c, the streamwise wavenumber α_c and the phase velocity s_c, remain relatively constant for the range of ϕ_∞ considered.

A second set of neutral stability curves is shown in figure 12(*b*), but for nanoparticles made of Al. Like the Cu nanoparticles, there is no vertical variation as ϕ_∞ increases. However, a small stabilising effect is observed, with neutral curves shifting to the right and marginally larger Reynolds numbers R. Therefore, the type of material used for the

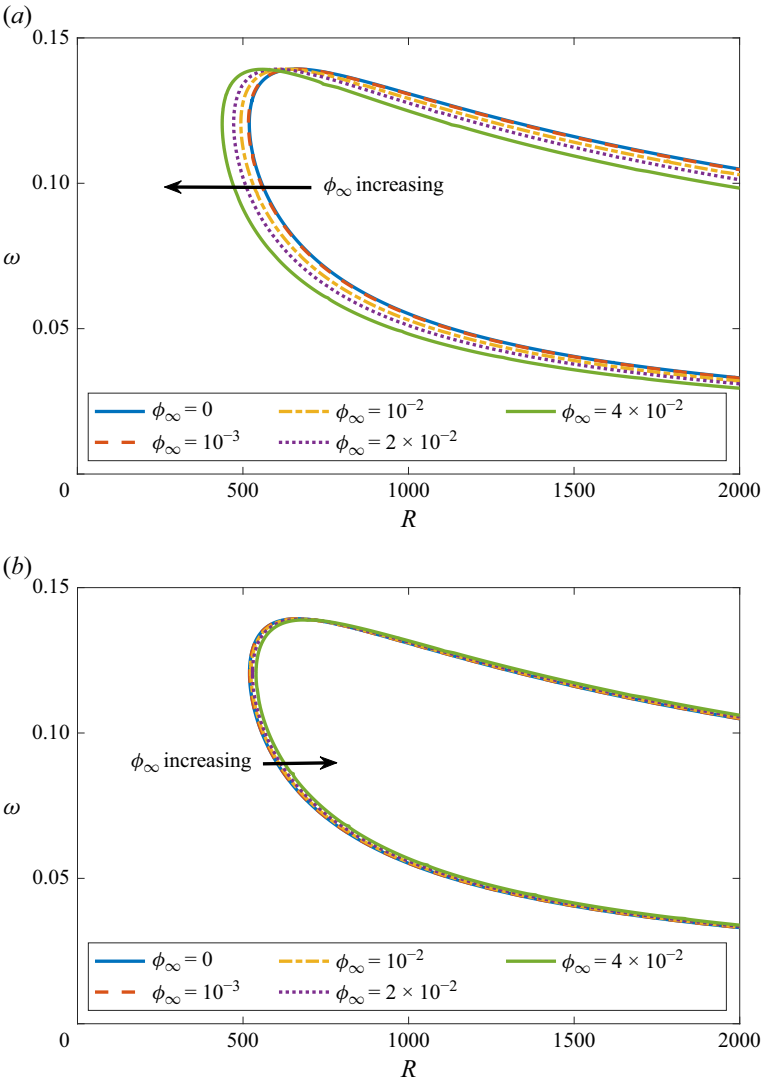

Figure 12. Neutral stability curves in the (R, ω)-plane for variable ϕ_∞, $\beta = 0$, $T_w = 2$ and (*a*) Cu nanoparticles and (*b*) Al nanoparticles.

nanoparticles plays a significant role in determining whether the TS wave is stabilised or destabilised.

Figure 13 presents further evidence of the stabilising benefits of Al nanoparticles compared with the destabilising effects of Cu nanoparticles. The circular (Cu) and diamond (Al) markers indicate the critical Reynolds numbers R_c obtained from the full linear stability equations (4.10), with a noticeable reduction in R_c for Cu nanoparticles and a small increase for Al nanoparticles. Additionally, the critical Reynolds number R_c for these two types of nanoparticles is plotted when BM and TP are neglected, as represented by the solid blue and dashed red curves. In this case, the critical Reynolds number $R_c = \mu \widehat{R}_c/\rho$, where $\widehat{R}_c \approx 519.4$ is the critical Reynolds number for the Blasius flow without nanoparticles. Thus, using the definition for density ρ and the Brinkman dynamic viscosity μ, given by (2.13*a*) and (2.14), respectively, the critical Reynolds for

ϕ_∞	Copper (Cu) R_c	Aluminium (Al) R_c
0	519.4	519.4
10^{-6}	519.4 (519.4)	519.4 (519.4)
10^{-5}	519.3 (519.3)	519.5 (519.5)
10^{-4}	519.2 (519.2)	519.5 (519.5)
10^{-3}	516.7 (516.7)	520.1 (519.9)
10^{-2}	493.7 (493.6)	523.9 (523.8)
2×10^{-2}	471.9 (471.6)	528.6 (528.3)
4×10^{-2}	437.5 (436.7)	539.2 (538.5)

Table 4. Critical Reynolds numbers R_c for Cu and Al nanoparticles in a base fluid of water, while the results in brackets correspond to the solutions obtained in the absence of BM and TP.

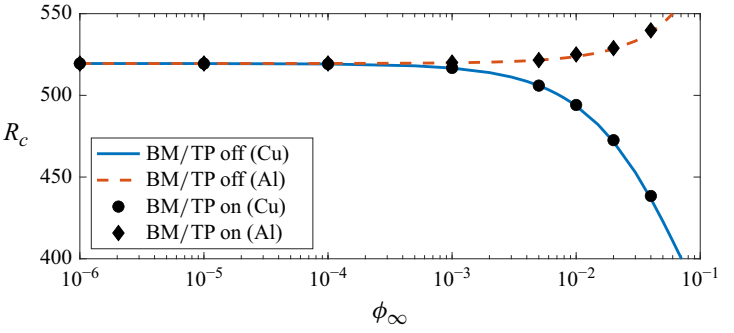

Figure 13. Critical Reynolds number R_c as a function of ϕ_∞, for Cu nanoparticles (solid blue line and circular markers) and Al nanoparticles (dashed red line and diamond markers) in a base fluid of water without (BM/TP off) and with (BM/TP on) BM and TP.

the nanofluid flow is approximated as

$$R_c = \frac{519.4}{(1-\phi_\infty)^{2.5}(1+(\hat{\rho}-1)\phi_\infty)}. \tag{4.14}$$

Unsurprisingly, the results with and without BM and TP are nearly identical. Thus, the impact of these diffusion effects on the linear stability of the nanofluid flow are negligible. Table 4 lists critical Reynolds numbers R_c at select ϕ_∞ values for both Cu and Al nanoparticles.

Consequently, the critical Reynolds number R_c is governed by the dynamic viscosity μ and the density ρ of the nanofluid, which are in turn influenced by the free stream nanofluid volume concentration ϕ_∞ and the ratio of densities $\hat{\rho}$. Figure 14 illustrates R_c as approximated by equation (4.14). In the first plot, figure 14(a), R_c is plotted as a function of ϕ_∞ and demonstrates the influence of both ϕ_∞ and the material used for the nanoparticles. Denser materials with larger $\hat{\rho}$ ratios, like Ag and Cu, have a destabilising effect, while lighter materials, like Si and Al, stabilise the flow. On the other hand, Al_2O_3 exhibits a marginally destabilising effect at small ϕ_∞, with a stabilising benefit realised for large ϕ_∞ (for $\phi_\infty \gtrapprox 0.09$).

Figure 14(b) further demonstrates the impact of nanofluids on the onset of linear instability, with R_c plotted in the $(\phi_\infty, \hat{\rho})$-plane. The solid red contour corresponds to $R_c = 519.4$ (i.e. the onset of linear instability in the standard Blasius flow), with solutions illustrating the negative impact of most nanoparticle materials, except Si and Al, on the

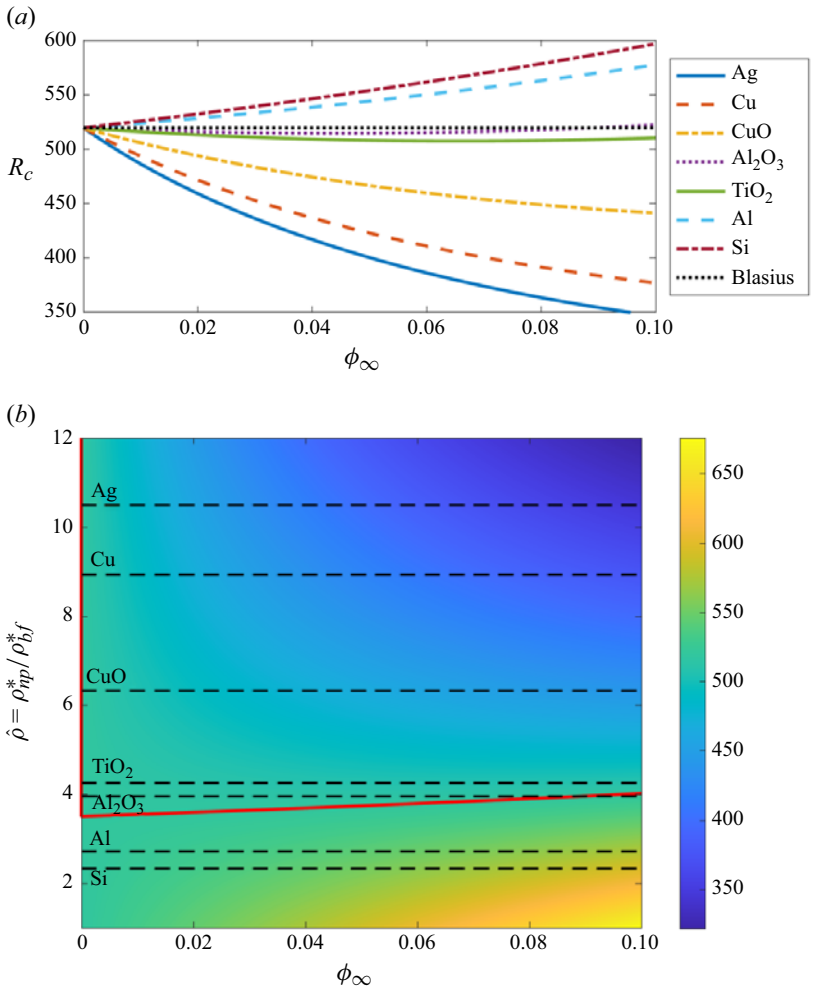

Figure 14. Plots of the critical Reynolds number R_c for the seven nanoparticle materials tabulated in table 1 in a base fluid of water, with the dynamic viscosity μ based on the Brinkman (1952) model (2.14). (*a*) Here R_c as a function of ϕ_∞. (*b*) Contours of R_c in the $(\phi_\infty, \hat{\rho})$-plane, where the solid red contour represents the contour level $R_c = 519.4$, matched to the critical conditions for the Blasius flow without nanoparticles.

hydrodynamic stability of the flow. More specifically, for a base fluid of water, only nanoparticles with a density ratio $\hat{\rho} \lessapprox 3.5$ are stabilising.

5. Asymptotic analysis

To describe the lower-branch structure of the neutral stability curve, we follow the approach of Smith (1979) and assume a large Reynolds number Re. Consequently, linear disturbances on the lower branch are governed by a triple deck structure with a main deck of thickness $O(Re^{-1/2})$, an upper deck of thickness $O(Re^{-3/8})$ and a lower deck of thickness $O(Re^{-5/8})$, with streamwise length $O(Re^{-3/8})$ and frequency $O(Re^{-1/4})$. A diagram of the triple deck structure is shown in figure 15 for $\varepsilon = Re^{-1/8}$. In addition,

$$x = 1 + \varepsilon^3 X \quad \text{and} \quad t = \varepsilon^2 \hat{t}, \tag{5.1a,b}$$

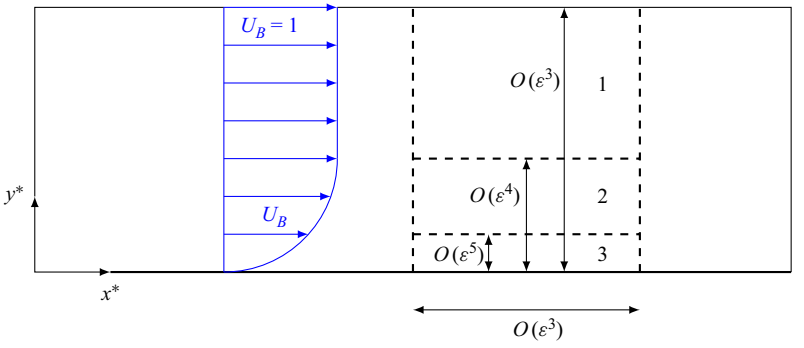

Figure 15. Diagram of the triple deck structure of the lower-branch of the neutral stability curve for $\varepsilon = Re^{-1/8}$. Regions 1, 2 and 3 correspond to the upper, main and lower decks, respectively.

while linear disturbances are taken to be proportional to

$$E = \exp\left(\mathrm{i}\left(\Theta(X) - \omega\hat{t}\right)\right), \tag{5.2a}$$

for

$$\frac{\mathrm{d}\theta}{\mathrm{d}X} = \alpha_1(x) + \varepsilon\alpha_2(x) + \cdots \quad \text{and} \quad \omega = \omega_1 + \varepsilon\omega_2 + \cdots. \tag{5.2b,c}$$

5.1. *The main deck*

Here $y = \varepsilon^4 y_2$, for $y_2 = O(1)$, where perturbations $\tilde{\boldsymbol{q}} = (\tilde{u}, \tilde{v}, \tilde{p}, \tilde{T}, \tilde{\phi})$ are expanded as

$$\begin{aligned}
\tilde{u} &= (u_2 + O(\varepsilon))\, E, \qquad \tilde{v} = \left(\varepsilon v_2 + O\left(\varepsilon^2\right)\right) E, \\
\tilde{p} &= \left(\varepsilon p_2 + O\left(\varepsilon^2\right)\right) E, \quad \tilde{T} = (T_2 + O(\varepsilon))\, E, \\
\tilde{\phi} &= (\phi_2 + O(\varepsilon))\, E,
\end{aligned} \tag{5.3a–e}$$

where $u_2 = u_2(x, y_2)$, etc. Similar expansions are given for the perturbed quantities $\tilde{\mu}$, $\tilde{\rho}$, $\tilde{c}$ and $\tilde{k}$. In addition, the nanoparticle volume concentration $\phi_B \sim \phi_\infty$.

Substituting (5.3) into the linear stability equations (4.3) and collecting the leading-order terms, gives the solution

$$u_2 = A(x)U_{B,y_2}, \quad v_2 = -\mathrm{i}\alpha_1 A(x)U_B \quad \text{and} \quad p_2 = p_2(x), \tag{5.4a–c}$$

where $p_2(x)$ and $A(x)$ are unknown, slowly varying, amplitude functions, representing pressure and negative displacement perturbations, respectively. Similarly,

$$T_2 = A(x)T_{B,y_2} \quad \text{and} \quad \phi_2 = 0. \tag{5.4d,e}$$

5.2. *The upper deck*

Here $y = \varepsilon^3 y_1$, for $y_1 = O(1)$. To match with the main deck, perturbations are expanded as

$$\tilde{u} = \left(\varepsilon u_1 + O\left(\varepsilon^2\right)\right) E, \quad \tilde{v} = \left(\varepsilon v_1 + O\left(\varepsilon^2\right)\right) E,$$
$$\tilde{p} = \left(\varepsilon p_1 + O\left(\varepsilon^2\right)\right) E, \quad \tilde{T} = \left(\varepsilon T_1 + O\left(\varepsilon^2\right)\right) E,$$
$$\tilde{\phi} = \left(\varepsilon \phi_1 + O\left(\varepsilon^2\right)\right) E, \tag{5.5a–e}$$

where $u_1 = u_1(x, y_1)$, etc. Similar expansions are again given for the perturbed quantities $\tilde{\mu}$, $\tilde{\rho}$, $\tilde{c}$ and $\tilde{k}$. In addition, the base flow is effectively given by the uniform free stream conditions

$$U_B \approx 1, \quad V_B \approx 0, \quad T_B \approx 1,$$
$$\phi_B \approx \phi_\infty, \quad c_B \approx c_\infty, \quad \rho_B \approx \rho_\infty. \tag{5.6a–f}$$

Substituting (5.5) and (5.6) into the linear stability equations (4.3), gives

$$\left(\frac{\partial^2}{\partial y_1} - \alpha_1^2\right) p_1 = 0, \tag{5.7}$$

with the bounded solution as $y_1 \to \infty$ given by

$$p_1 = P_1(x) \mathrm{e}^{-\alpha_1 y_1}, \tag{5.8a}$$

where $P_1(x)$ is an unknown function of x and $\alpha_1 > 0$. Moreover,

$$u_1 = -\frac{P_1(x)\mathrm{e}^{-\alpha_1 y_1}}{\rho_\infty}, \quad v_1 = -\frac{\mathrm{i} P_1(x)\mathrm{e}^{-\alpha_1 y_1}}{\rho_\infty}, \quad T_1 = 0 \quad \text{and} \quad \phi_1 = 0. \tag{5.8b–e}$$

Continuity of pressure requires

$$P_1(x) = p_2(x) \quad \text{as} \quad y_1 \to 0. \tag{5.9}$$

Similarly, continuity of the wall-normal velocity $\tilde{v}$ between the main deck solution (5.4*b*) and the upper deck solution (5.8*c*) yields the condition

$$\alpha_1 A(x) = \frac{p_2(x)}{\rho_\infty}. \tag{5.10}$$

5.3. *The lower deck*

Recall that the concentration layer has a characteristic thickness of $O(Re^{-1/2}Sc^{-1/3})$. By setting $Sc^{-1/3} \sim Re^{-1/8}$, the lower deck coincides with the concentration layer.

To match with the main deck, in the lower deck $y = \varepsilon^5 y_3$, for $y_3 = O(1)$. Perturbations in the lower deck are then expanded as

$$\tilde{u} = \left(u_3 + O(\varepsilon)\right) E, \quad \tilde{v} = \left(\varepsilon^2 v_3 + O\left(\varepsilon^3\right)\right) E,$$
$$\tilde{p} = \left(\varepsilon p_3 + O\left(\varepsilon^2\right)\right) E, \quad \tilde{T} = \left(T_3 + O(\varepsilon)\right) E,$$
$$\tilde{\phi} = \left(\phi_3 + O(\varepsilon)\right) E, \tag{5.11a–e}$$

where $u_3 = u_3(x, y_3)$, etc. As before, similar expansions are introduced for the perturbed quantities $\tilde{\mu}$, $\tilde{\rho}$, $\tilde{c}$ and $\tilde{k}$.

In the main deck, the base velocity behaves as $U_B \sim \lambda y_2$ as $y_2 \to 0$, where $\lambda = U_{B,y_2}|_{y_2=0} (\equiv \rho_w f''(0)/x^{1/2})$, and consequently from (5.4*a*) and (5.4*b*)

$$u_2 \to \lambda A(x) \quad \text{and} \quad v_2 \to -\mathrm{i}\alpha_1 \lambda A(x) y_2 \quad \text{as} \quad y_2 \to 0. \tag{5.12a,b}$$

Therefore, within the lower deck, the base flow is given by

$$U_B = \varepsilon\lambda y_3 + O\left(\varepsilon^2\right), \qquad V_B = -\frac{1}{2}\varepsilon^2\lambda_x y_3^2 + O\left(\varepsilon^3\right),$$
$$T_B = T_w + \varepsilon\sigma y_3 + O\left(\varepsilon^2\right), \qquad \phi_B = \phi_\infty + \varepsilon\psi(x, y_3) + O\left(\varepsilon^2\right), \tag{5.13a–d}$$

where $\sigma = T_{B,y_2}|_{y_2=0} (\equiv \rho_w\theta'(0)/x^{1/2})$.

Substituting (5.11) and (5.13) into the linear stability equations (4.3) gives

$$p_3 = p_2(x), \tag{5.14}$$

to match with the pressure in the main deck, and

$$u_3 = B(x)\int_{\chi_0}^{\chi} \mathrm{Ai}(\grave{\chi})\,\mathrm{d}\grave{\chi}, \tag{5.15a}$$

$$p_2 = -\frac{\omega_1\rho_\infty}{\alpha_1}\frac{B(x)\mathrm{Ai}'(\chi_0)}{\chi_0}, \tag{5.15b}$$

where B is an unknown, amplitude function, Ai is the Airy function and

$$\chi = \left(\frac{\mathrm{i}\alpha_1\lambda\rho_\infty}{\mu_\infty}\right)^{1/3}\left(y_3 - \frac{\omega_1}{\alpha_1\lambda}\right), \tag{5.16}$$

for $\chi_0 = \chi|_{y_3=0}$.

Matching the streamwise velocity $\tilde{u}$ between the main deck solution (5.12*a*) and the lower deck solution (5.15*a*), gives

$$B(x)\int_{\chi_0}^{\infty} \mathrm{Ai}(\chi)\,\mathrm{d}\chi = \lambda A(x). \tag{5.17}$$

Eliminating A, B and p_2 from (5.10), (5.15*b*) and (5.17) yields the leading-order eigenrelation

$$\frac{\mathrm{Ai}'(\chi_0)}{\int_{\chi_0}^{\infty}\mathrm{Ai}(\chi)\,\mathrm{d}\chi} = \left(\frac{\mathrm{i}\alpha_1\lambda\rho_\infty}{\mu_\infty}\right)^{1/3}\frac{\alpha_1}{\lambda^2}, \tag{5.18a,b}$$

which, following the parameter scaling

$$\alpha_1 = \lambda^{5/4}\left(\frac{\mu_\infty}{\rho_\infty}\right)^{1/4}\overline{\alpha} \quad \text{and} \quad \omega_1 = \lambda^{3/2}\left(\frac{\mu_\infty}{\rho_\infty}\right)^{1/2}\overline{\omega}, \tag{5.19a}$$

becomes

$$\frac{\mathrm{Ai}'(\chi_0)}{\int_{\chi_0}^{\infty}\mathrm{Ai}(\chi)\,\mathrm{d}\chi} = \mathrm{i}^{1/3}\overline{\alpha}^{4/3} \quad \text{for} \quad \chi_0 = -\mathrm{i}^{1/3}\frac{\overline{\omega}}{\overline{\alpha}^{2/3}}. \tag{5.20a,b}$$

For neutral stability, α_1, α_2, etc. must be real, requiring $\chi_0 = -2.298\mathrm{i}^{1/3}$ and

$$\frac{\mathrm{Ai}'(\chi_0)}{\int_{\chi_0}^{\infty}\mathrm{Ai}(\chi)\,\mathrm{d}\chi} = 1.001\mathrm{i}^{1/3}. \tag{5.21}$$

Consequently, the neutral values of α_1 and ω_1 are given as

$$\alpha_1 = 1.001\hat{\lambda}^{5/4}\left(\frac{\mu_\infty}{\rho_\infty}\right)^{1/4}x^{-5/8}, \tag{5.22a}$$

$$\omega_1 = 2.299\hat{\lambda}^{3/2}\left(\frac{\mu_\infty}{\rho_\infty}\right)^{1/2}x^{-3/4}, \tag{5.22b}$$

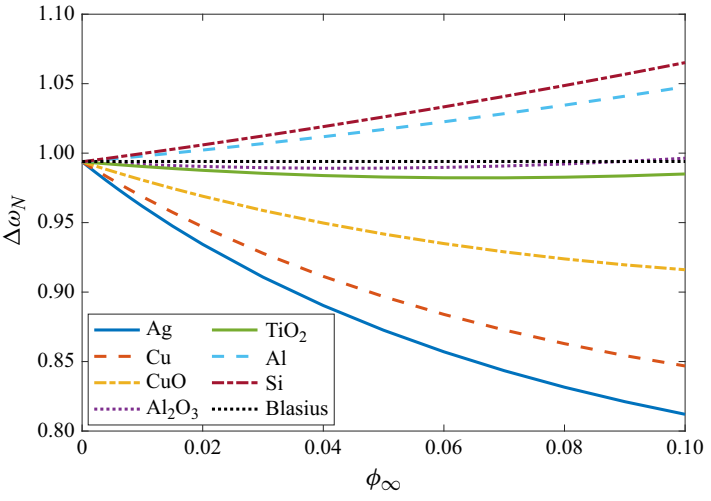

Figure 16. Gradient $\Delta\omega_N = 0.994[\mu_\infty/\rho_\infty]^{1/2}$ of the lower branch (5.23) as a function of ϕ_∞ for different nanoparticle materials.

where $\hat{\lambda} = \rho_w f''(0)$. This gives the leading-order approximation for the frequency of the lower branch in terms of the Reynolds number Re:

$$\omega_N \sim 2.299[\delta_1\hat{\lambda}]^{3/2}\left(\frac{\mu_\infty}{\rho_\infty}\right)^{1/2} Re^{-1/2}. \tag{5.23}$$

Notably, in the limit $Sc \to \infty$, $\delta_1\hat{\lambda} \approx 0.572$ across all nanoparticle materials and ϕ_∞. Thus, $2.299[\delta_1\hat{\lambda}]^{3/2} \approx 0.994$.

Figure 16 depicts the gradient of the frequency ω_N, defined as $\Delta\omega_N = 0.994[\mu_\infty/\rho_\infty]^{1/2}$, as a function of ϕ_∞ for all seven nanoparticle materials listed in table 1. A gradient $\Delta\omega_N < 0.994$ indicates a destabilising effect, while $\Delta\omega_N > 0.994$ corresponds to stabilising behaviour. The solutions are qualitatively similar to and consistent with the linear stability results shown in figure 14(*a*): less dense materials are stabilising and denser materials are destabilising.

6. Conclusions

A linear stability study has been conducted on the nanofluid boundary-layer flow over a flat plate, extending the earlier work of Buongiorno (2006), Avramenko *et al.* (2011), MacDevette *et al.* (2014) and Turkyilmazoglu (2020). The model employs a two-phase flow formulation that incorporates the effects of BM and TP, with all quantities scaled on the base fluid characteristics, providing a physically consistent approach for investigating stability trends. Although the influence of BM and TP is relatively weak, a thin concentration layer with a characteristic thickness of $O(Re^{-1/2}Sc^{-1/3})$ develops within the boundary layer, which modifies the near-wall velocity and temperature fields. The concentration layer disappears when BM and TP are ignored, with the nanoparticle volume concentration ϕ uniform throughout the boundary layer.

In terms of thermodynamic performance, all seven materials modelled herein establish an increasing Nusselt number Nu, with greater benefits obtained for denser materials like Ag and Cu.

Despite the emergence of a thin concentration layer, numerical and asymptotic stability calculations show that BM and TP have a negligible impact on the onset of the TS wave. In fact, linear stability characteristics and the onset of TS waves can be accurately predicted using solutions to the standard Blasius flow, which effectively models the nanofluid flow as a single-phase fluid. The Reynolds number for the nanofluid is given as

$$Re = \frac{\mu \widehat{Re}}{\rho}, \tag{6.1}$$

for the Blasius flow Reynolds number $\widehat{Re}$. Consequently, the stability of the nanofluid boundary-layer flow is governed by the density ρ and viscosity μ of the nanofluid. In particular, the density ratio $\hat{\rho} = \rho^*_{np}/\rho^*_{bf}$ is critical to determining whether the nanofluid is stabilising or destabilising. Denser nanoparticle materials, such as Ag and Cu, significantly destabilise the TS wave. In contrast, a small stabilising effect is achieved by lighter materials, like Al and Si. This observation differs from the one-phase flow study conducted by Turkyilmazoglu (2020), which predicted the opposite outcome. However, in Turkyilmazoglu's investigation, physical quantities were scaled on the characteristics of the nanofluid rather than the base fluid, leading to a Reynolds number that varied with the type of nanoparticle material and volume concentration.

The results presented above are based on a nanofluid with water as the base fluid. Replacing water with a less dense fluid, like ethanol, would increase the density ratio $\hat{\rho}$ for all materials. While this change would enhance the thermal benefits of the nanofluid, it would lead to a further destabilisation of the TS wave, even for those nanofluids composed of lighter materials like Al and Si.

Another key factor influencing nanofluid stability is the choice of viscosity model. The above study adopted the Brinkman (1952) model (2.5) to represent the nanofluids dynamic viscosity, ensuring consistency with earlier investigations. However, alternative models can produce very different results. For instance, the correlations due to Pak & Cho (1998) and Maiga *et al.* (2004) in pipe and tube flows (see (2.6*b*)) predict larger increases in viscosity as the nanoparticle volume concentration ϕ increases. Assuming these models can be applied to the boundary-layer flow on a flat plate, the corresponding stability calculations based on (6.1) indicate a strong stabilising effect for all nanoparticle materials, in contrast to the destabilising trends observed for the Brinkman model. Since the Reynolds number and resulting stability characteristics depend on the viscosity model, accurately determining μ is crucial. The variety of models summarised in Wang & Mujumdar (2008*a*) and Mishra *et al.* (2014), including those that include nanoparticle aggregation, size and shape effects, and temperature-dependent viscosity, highlights the need for further experimental measurements of nanofluid viscosity in boundary-layer flows to enable the selection of the correct model and ensure physically accurate stability predictions.

In addition to a base fluid of water, nanoparticles were assumed to have a diameter of $d_{np} = 20\,\text{nm}$ with a free stream temperature $T_\infty = 300\,\text{K}$. Varying the nanoparticle diameter over the range $d_{np} = 1\,\text{nm}$ to $d_{np} = 100\,\text{nm}$ yields Schmidt numbers Sc ranging from approximately $O(10^3)$ to $O(10^5)$. Even at the lower end of this range, Sc is sufficiently large that BM and TP effects remain negligible. Furthermore, applying the analysis to an ethanol-based fluid establishes comparable Sc values, whereas an oil-based fluid results in even larger values due to its higher viscosity. While increasing T_∞ can reduce Sc to $O(10^2)$ for $T_\infty = 1000\,\text{K}$, such high temperatures are generally unrealistic for practical nanofluid applications.

Future investigations into nanofluid boundary-layer flows could include non-parallel and nonlinear stability effects by using parabolised stability equations, following the approach

of Bertolotti *et al.* (1992). Additionally, the analysis may be applied to other geometries, including rotating disk boundary layers and wall jets, as considered by Turkyilmazoglu (2020). However, based on the observations above, we anticipate that the stability trends would remain similar: heavier nanoparticles are expected to be destabilising, lighter nanoparticles stabilising, with the flows well-approximated by the standard Blasius flow without nanoparticles.

Acknowledgements. J.S.B.G. is grateful to the Sydney Mathematics Research Institute (SMRI) for financial support and for hosting a trip to the SMRI as a visiting researcher during July and August 2023, which helped facilitate this research project.

Declaration of interests. The authors report no conflict of interest.

Appendix A. On ignoring BM and TP

When the effects of BM and TP are ignored, the continuity equation for the nanoparticles, given by (2.1*d*), reduces to the form

$$\frac{\partial \phi}{\partial t^*} + \phi \nabla^* \cdot \boldsymbol{u}^* + \nabla^* \phi \cdot \boldsymbol{u}^* = 0. \tag{A1}$$

In addition, the continuity (2.1*a*) can be rewritten in the form

$$\frac{\partial \rho^*}{\partial t^*} + \rho^* \nabla^* \cdot \boldsymbol{u}^* + \nabla^* \rho^* \cdot \boldsymbol{u}^* = 0, \tag{A2}$$

which on using the definition for density (2.2) becomes

$$\left(\rho^*_{np} - \rho^*_{bf}\right)\left(\frac{\partial \phi}{\partial t^*} + \nabla^* \phi \cdot \boldsymbol{u}^*\right) + \rho^* \nabla^* \cdot \boldsymbol{u}^* = 0. \tag{A3}$$

Subsequently, combining (A1) and (A3) gives

$$\left(\left(\rho^*_{bf} - \rho^*_{np}\right)\phi + \rho^*\right) \nabla^* \cdot \boldsymbol{u}^* = 0, \tag{A4}$$

which implies the flow is incompressible,

$$\nabla^* \cdot \boldsymbol{u}^* = 0, \tag{A5}$$

and the continuity equation for the nanoparticles (A1) reduces to

$$\frac{\partial \phi}{\partial t^*} + \nabla^* \phi \cdot \boldsymbol{u}^* = 0. \tag{A6}$$

Consequently, the Prandtl scaling in § 3.1 gives

$$\phi' = 0 \quad \text{with} \quad \phi \to \phi_\infty \quad \text{as} \quad y \to \infty. \tag{A7}$$

Thus, $\phi = \phi_\infty$ for all y, i.e. ϕ is a constant. Hence, base flow quantities, including the viscosity μ, density ρ, specific heat capacity c and thermal conductivity k are constant.

On coupling the scalings (2.11) with the following substitutions:

$$p = \rho \hat{p}, \quad T = 1 + (T_w - 1)\widehat{T}, \quad \widehat{Re} = \frac{\rho}{\mu} Re, \quad \widehat{Pr} = \frac{\mu c}{k} Pr, \tag{A8}$$

transforms the non-dimensional governing equations (2.12) into the form

$$\boldsymbol{\nabla} \cdot \boldsymbol{u} = 0, \tag{A9a}$$

$$\frac{\partial \boldsymbol{u}}{\partial t} + (\boldsymbol{u} \cdot \boldsymbol{\nabla})\boldsymbol{u} = -\boldsymbol{\nabla} \hat{p} + \frac{1}{\widehat{Re}} \nabla^2 \boldsymbol{u}, \tag{A9b}$$

$$\frac{\partial \widehat{T}}{\partial t} + (\boldsymbol{u}\cdot\boldsymbol{\nabla})\widehat{T} = \frac{1}{\widehat{Re}\widehat{Pr}}\nabla^2\widehat{T}, \tag{A9c}$$

for boundary conditions

$$\boldsymbol{u} = 0 \quad \text{and} \quad \widehat{T} = 1 \quad \text{on} \quad y = 0, \tag{A10a,b}$$

and

$$\begin{aligned} &u \to 1, \quad v \to 0, \quad w \to 0, \\ &\hat{p} \to 0, \quad \widehat{T} \to 0, \quad \phi \to \phi_\infty \quad \text{as} \quad y \to \infty. \end{aligned} \tag{A11a–f}$$

Subsequently, applying the Prandtl transformation for $\widehat{Re} \to \infty$ establishes the Blasius boundary-layer equations (3.9), with an equivalent set of linear stability equations for the Reynolds number $\widehat{Re}$. Thus, when BM and TP are neglected, the linear stability of the nanofluid flow reduces to the Blasius flow, with the nanofluid Reynolds number given as $Re = \mu\widehat{Re}/\rho$.

Appendix B. Base flow and perturbation quantities

B.1. *Terms in (4.3)*

The functions $g_\star$ in the linear stability equations (4.3) are given as

$$g_1(V_B,\, \boldsymbol{Q}_{B,x}) = -\left(\rho_{B,x}\tilde{u} + U_{B,x}\tilde{\rho} + Re^{-1/2}\frac{\partial}{\partial y}\left(V_B\tilde{\rho}\right)\right), \tag{B1a}$$

$$\begin{aligned} g_2(V_B,\, \boldsymbol{Q}_{B,x}) = \frac{1}{Re}\Bigg(&\mu_{B,x}\left(\frac{4}{3}\frac{\partial \tilde{u}}{\partial x} - \frac{2}{3}\left(\frac{\partial \tilde{v}}{\partial y} + \frac{\partial \tilde{w}}{\partial z}\right)\right) \\ &+ \frac{\partial}{\partial x}\left(\left(\frac{4}{3}U_{B,x} - \frac{2}{3}Re^{-1/2}V_{B,y}\right)\tilde{\mu}\right) + Re^{-1/2}\frac{\partial}{\partial y}\left(V_{B,x}\tilde{\mu}\right)\Bigg) \\ &- \left(U_{B,x}\left(\rho_B\tilde{u} + U_B\tilde{\rho}\right) - Re^{-1/2}V_B\left(\rho_B\frac{\partial \tilde{u}}{\partial y} + U_{B,y}\tilde{\rho}\right)\right), \end{aligned} \tag{B1b}$$

$$\begin{aligned} g_3(V_B,\, \boldsymbol{Q}_{B,x}) = \frac{1}{Re}\Bigg(&\mu_{B,x}\left(\frac{\partial \tilde{v}}{\partial x} + \frac{\partial \tilde{u}}{\partial y}\right) + \frac{\partial}{\partial y}\left(\left(\frac{4}{3}Re^{-1/2}V_{B,y} - \frac{2}{3}U_{B,x}\right)\tilde{\mu}\right) \\ &+ Re^{-1/2}\frac{\partial}{\partial x}\left(V_{B,x}\tilde{\mu}\right)\Bigg) - Re^{-1/2}\Bigg(V_{B,x}\left(\rho_B\tilde{u} + U_B\tilde{\rho}\right) \\ &+ V_B\left(\rho_B\frac{\partial \tilde{v}}{\partial y} - Re^{-1/2}V_{B,y}\tilde{\rho}\right) + \rho_B V_{B,y}\tilde{v}\Bigg), \end{aligned} \tag{B1c}$$

$$\begin{aligned} g_4(V_B,\, \boldsymbol{Q}_{B,x}) = \frac{1}{Re}\Bigg(&\mu_{B,x}\left(\frac{\partial \tilde{w}}{\partial x} + \frac{\partial \tilde{u}}{\partial z}\right) - \frac{2}{3}\frac{\partial}{\partial z}\left(\left(U_{B,x} + Re^{-1/2}V_{B,y}\right)\tilde{\mu}\right)\Bigg) \\ &- Re^{-1/2}\rho_B V_B\frac{\partial \tilde{w}}{\partial y}, \end{aligned} \tag{B1d}$$

$$\begin{aligned} g_5(V_B,\, \boldsymbol{Q}_{B,x}) = &\frac{1}{RePr}\left(k_{B,x}\frac{\partial \tilde{T}}{\partial x} + T_{B,x}\frac{\partial \tilde{k}}{\partial x} + T_{B,xx}\tilde{k}\right) + \frac{1}{RePrLe}\Bigg(T_{B,x}\phi_{B,x}\tilde{T} \\ &+ T_B\left(T_{B,x}\frac{\partial \tilde{\phi}}{\partial x} + \phi_{B,x}\frac{\partial \tilde{T}}{\partial x}\right) + \frac{1}{N_{BT}T_B}\left(2\phi_B T_{B,x}\frac{\partial \tilde{T}}{\partial x} + T_{B,x}^2\left(\tilde{\phi} - \frac{\phi_B\tilde{T}}{T_B}\right)\right)\Bigg) \end{aligned}$$

$$- \left(\rho_B T_B c_{B,x}\tilde{u} + U_B c_{B,x}\left(T_B\tilde{\rho} + \rho_B\tilde{T}\right) + (\rho c)_B T_{B,x}\tilde{u} + U_B T_{B,x}\tilde{\rho}\tilde{c}\right)$$
$$- Re^{-1/2}V_B\left(\rho_B T_B\frac{\partial\tilde{c}}{\partial y} + c_{B,y}\left(T_B\tilde{\rho} + \rho_B\tilde{T}\right) + (\rho c)_B\frac{\partial\tilde{T}}{\partial y} + T_{B,y}\tilde{\rho}\tilde{c}\right), \tag{B1e}$$

$$g_6(V_B,\, \boldsymbol{Q}_{B,x}) = \frac{1}{ReSc}\left(T_{B,x}\frac{\partial\tilde{\phi}}{\partial x} + \phi_{B,xx}\tilde{T} + \phi_{B,x}\frac{\partial\tilde{T}}{\partial x}\right)$$
$$+ \frac{1}{ReScN_{BT}}\left(\left(\frac{\phi_{B,x}}{T_B} - \frac{\phi_B T_{B,x}}{T_B^2}\right)\frac{\partial\tilde{T}}{\partial x} - T_{B,xx}\left(\frac{\tilde{\phi}}{T_B} - \frac{\phi_B\tilde{T}}{T_B^2}\right)\right.$$
$$\left. + T_{B,x}\left(\frac{1}{T_B}\frac{\partial\tilde{\phi}}{\partial x} - \frac{T_{B,x}}{T_B^2}\tilde{\phi} - \frac{\phi_B}{T_B^2}\frac{\partial\tilde{T}}{\partial x} + \left(\frac{2\phi_B T_{B,x}}{T_B^3} - \frac{\phi_{B,x}}{T_B^2}\right)\tilde{T}\right)\right)$$
$$- \phi_{B,x}\tilde{u} - U_{B,x}\tilde{\phi} - Re^{-1/2}\left(V_B\frac{\partial\tilde{\phi}}{\partial y} + V_{B,y}\tilde{\phi}\right). \tag{B1f}$$

B.2. *Terms in (4.10)*

The base flow quantities in the system of equations (4.10) are given as

$$\rho_B = 1 + (\hat{\rho} - 1)\phi_B, \qquad \rho_{B,y} = (\hat{\rho} - 1)\phi_{B,y},$$
$$(\rho c)_B = 1 + (\hat{\rho}\hat{c} - 1)\phi_B,$$
$$c_B = \frac{(\rho c)_B}{\rho_B}, \qquad c_{B,y} = \frac{\hat{\rho}(\hat{c} - 1)\phi_{B,y}}{\rho_B^2},$$
$$\mu_B = \frac{1}{(1 - \phi_B)^{2.5}}, \qquad \mu_{B,y} = \frac{2.5\mu_B\phi_{B,y}}{1 - \phi_B},$$
$$k_B = \frac{\hat{k} + 2 + 2(\hat{k} - 1)\phi_B}{\hat{k} + 2 - (\hat{k} - 1)\phi_B}, \qquad k_{B,y} = \mathcal{K}\phi_{B,y}, \tag{B2a–i}$$

and the perturbation quantities are given as

$$\breve{\rho} = (\hat{\rho} - 1)\breve{\phi},$$
$$(\breve{\rho}\breve{c}) = (\hat{\rho}\hat{c} - 1)\breve{\phi}, \qquad \breve{c} = \frac{\hat{\rho}(\hat{c} - 1)\breve{\phi}}{\rho_B^2},$$
$$\breve{\mu} = \frac{2.5\mu_B\breve{\phi}}{1 - \phi_B}, \qquad \mathrm{D}\breve{\mu} = \frac{2.5\mu_B}{1 - \phi_B}\left(\mathrm{D} + \frac{3.5\phi_{B,y}}{1 - \phi_B}\right)\breve{\phi},$$
$$\breve{k} = \mathcal{K}\breve{\phi}, \qquad \mathrm{D}\breve{k} = \mathcal{K}\left(\mathrm{D} + \frac{2(\hat{k} - 1)\phi_{B,y}}{\hat{k} + 2 - (\hat{k} - 1)\phi_B}\right)\breve{\phi}, \tag{B3a–g}$$

where

$$\mathcal{K} = \frac{3(\hat{k} - 1)(\hat{k} + 2)}{(\hat{k} + 2 - (\hat{k} - 1)\phi_B)^2}. \tag{B4}$$

Appendix C. Effect of wall temperature

The linear stability analysis in § 4 was presented for the case $T_w = 2$. Figure 17 shows the real and imaginary parts of the TS wave frequency ω as a function of T_w for $R = 500$,

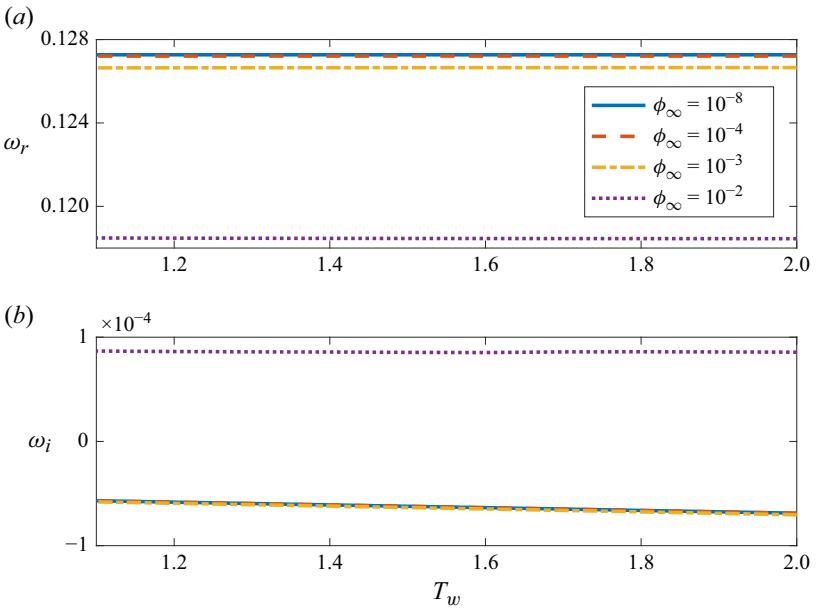

Figure 17. Frequency $\omega = \omega_r + \mathrm{i}\omega_i$ as a function of the wall temperature T_w for $R = 500$, $\alpha = 0.3$, $\beta = 0$ and $\phi_\infty \in [10^{-8}, 10^{-2}]$. (*a*) Real part and (*b*) imaginary part.

$\alpha = 0.3$, $\beta = 0$ and variable ϕ_∞. The solutions exhibit negligible variations across the range of T_w considered, which is to be expected, since when BM and TP effects are ignored (both of which have been shown to be negligible), the analysis reduces via the substitution (3.8) to the standard Blasius flow, in which the wall temperature is removed from the formulation.

References

Avramenko, A.A., Blinov, D.G. & Shevchuk, I.V. 2011 Self-similar analysis of fluid flow and heat-mass transfer of nanofluids in boundary layer. *Phys. Fluids* **23**, 082002.

Bachok, N., Ishak, A. & Pop, I. 2011 Flow and heat transfer over a rotating porous disk in a nanofluid. *Physica B* **406**, 1767–1772.

Bahiraei, M. & Heshmatian, S. 2018 Electronics cooling with nanofluids: a critical review. *Energy Convers. Manage.* **172**, 438–456.

Barry, M.D.J. & Ross, M.A.S. 1970 The flat plate boundary layer. Part 2. The effect of increasing thickness on stability. *J. Fluid Mech.* **43**, 813–818.

Batchelor, G.K. 1977 The effect of Brownian motion on the bulk stress in a suspension of spherical particles. *J. Fluid Mech.* **83**, 97–117.

Bertolotti, F.P., Herbert, T. & Spalart, P.R. 1992 Linear and nonlinear stability of the Blasius boundary layer. *J. Fluid Mech.* **242**, 441–474.

Blasius, H. 1908 Grenzschichten in Flussigkeiten mit Kleiner Reibung. *Z. Angew. Math. Phys.* **56**, 1–37.

Bodonyi, R.J. & Smith, F.T. 1981 The upper branch stability of the Blasius boundary layer, including non-parallel flow effects. *Proc. R. Soc. Lond. A* **375**, 65–92.

Brinkman, H.C. 1952 The viscosity of concentrated suspensions and solutions. *J. Chem. Phys.* **20**, 571–581.

Buongiorno, J. 2006 Convective transport in nanofluids. *J. Heat Transfer* **128**, 240–250.

Buongiorno, J. & Hu, L.W. 2009 Nanofluid heat transfer enhancement for nuclear reactor applications. In *ASME 2009 Second International Conference on Micro/Nanoscale Heat and Mass Transfer*, vol. 3, pp. 517–522. AMSE.

Choi, S.U.S. 1995 Enhancing thermal conductivity of fluids with nanoparticles. In *Developments and Applications of Non-Newtonian Flows* (ed. D.A. Siginer & H.P. Wang), FED-vol. 231/MD-vol. 66, pp. 99–105. ASME.

DAS, S.K., CHOI, S.U.S. & PATEL, H.E. 2006 Heat transfer in nanofluids—A review. *Heat Transfer Engng* **27** (10), 3–19.

EINSTEIN, A. 1906 Eine neue Bestimmung der Moleküldimensionen. *Ann. Phys.* **19**, 289–306.

GANDHI, R., NEPOMNYASHCHY, A. & ORON, A. 2025 Thermosolutal instabilities in a moderately dense nanoparticle suspension. *J. Fluid Mech.* **1011**, A52.

GASTER, M. 1974 On the effects of boundary-layer growth on flow stability. *J. Fluid Mech.* **66**, 465–480.

GRIFFITHS, P.T., GALLACHER, M.T. & STEPHEN, S.O. 2016 The effect of non-Newtonian viscosity on the stability of the Blasius boundary layer. *Phys. Fluids* **28**, 074107.

GROSCH, C.E. & SALWEN, H. 1978 The continuous spectrum of the Orr–Sommerfeld equation. Part 1. The spectrum and the eigenfunctions. *J. Fluid Mech.* **87** (1), 33–54.

HEALEY, J.J. 1995 On the neutral curve of the flat-plate boundary layer: comparison between experiment, Orr–Sommerfeld theory and asymptotic theory. *J. Fluid Mech.* **288**, 59–73.

JORDINSON, R. 1970 The flat plate boundary layer. Part 1. Numerical integration of the Orr–Sommerfeld equation. *J. Fluid Mech.* **43**, 810–811.

KAKAÇ, S. & PRAMUANJAROENKIJ, A. 2009 Review of convective heat transfer enhancement with nanofluids. *Intl J. Heat Mass Transfer* **52** (13), 3187–3196.

KHULLAR, V., TYAGI, H., PHELAN, P.E., OTANICAR, T.P., SINGH, H. & TAYLOR, R.A. 2012 Solar energy harvesting using nanofluids-based concentrating solar collector. *ASME. J. Nanotechnolgy Engng Med.* **3** (3), 031003.

KUZNETSOV, A.V. & NIELD, D.A. 2010 Natural convective boundary-layer flow of a nanofluid past a vertical plate. *Intl J. Therm. Sci.* **49** (2), 243–247.

LAOUER, A., ALQURASHI, F., TEGGAR, M., AL-FARHANY, K., AHMED, S.E., ABDULKADHIM, A. & KCHAOU, M. 2024 Linear stability analysis of nanofluid flow over static or moving wedge using the collocation spectral method. *J. Engng Res.* **12**, 281–288.

LIN, C.C. 1955 *The Theory of Hydrodynamic Stability*. Cambridge University Press.

MACDEVETTE, M.M., MYERS, T.G. & WETTON, B. 2014 Boundary layer analysis and heat transfer of a nanofluid. *Microfluid Nanofluid* **17**, 401–412.

MACK, L.M. 1976 A numerical study of the temporal eigenvalue spectrum of the Blasius boundary layer. *J. Fluid Mech.* **73**, 497–520.

MACK, L.M. 1984 Boundary-layer linear stability theory. *Tech. Rep.* NASA-CR-3796. NASA.

MAHBUBUL, I.M., SAIDUR, R. & AMALINA, M.A. 2012 Latest developments on the viscosity of nanofluids. *Intl J. Heat Mass Transfer* **55**, 874–885.

MAIGA, S.E.B., NGUYEN, C.T., GALANIS, N. & ROY, G. 2004 Heat transfer behaviours of nanofluids in a uniformly heated tube. *Superlattices Microstructures* **35**, 543–557.

MAXWELL, J.C. 1881 *Treatise On Electricity and Magnetism*. Oxford University Press.

MCNAB, G.S. & MEISEN, A. 1973 Thermophoresis in liquids. *J. Colloid Interface Sci.* **44** (2), 339–346.

MEHMOOD, A. & USMAN, M. 2018 Heat transfer enhancement in rotating disk boundary-layer. *Therm. Sci.* **22**, 2467–2482.

MILLER, R., GARRETT, S.J., GRIFFITHS, P.T. & HUSSAIN, Z. 2018 Stability of the Blasius boundary layer over a heated plate in a temperature-dependent viscosity flow. *Phys. Rev. Fluids* **3**, 113902.

MISHRA, P.C., MUKHERJEE, S., NAYAK, S.K. & PANDA, A. 2014 A brief review on viscosity of nanofluids. *Intl Nano Lett.* **4**, 109–120.

PAK, B.C. & CHO, Y.I. 1998 Hydrodynamc and heat transfer study of dispersed fluids with submicron metallic oxide particles. *Exp. Heat Transfer Intl J.* **11**, 151–170.

PELEKASIS, N.A. & ACRIVOS, A. 1995 Forced convection and sedimentation past a flat plate. *J. Fluid Mech.* **294**, 301–321.

REDDY, J.R., DEEPTHI, V.V., RADJU, R.S., REDDY, B.M. & ALI, F. 2025 Computational modelling of thermal and mass transport in MHD nanofluid flow across a non-linear surface with chemical response and viscous dissipation. *Model. Earth Syst. Environ.* **11**, 254.

ROSS, J.A., BARNES, F.H., BURNS, J.G. & ROSS, M.A.S. 1970 The flat plate boundary layer. Part 3. Comparison of theory with experiment. *J. Fluid Mech.* **43**, 819–832.

RUBAN, A.I. 2017 *Fluid Dynamics Part 3: Boundary Layers*. Oxford University Press.

RUBAN, A.I. & GAJJAR, J.S.B. 2014 *Fluid Dynamics Part 1: Classical Fluid Dynamics*. Oxford University Press.

SALWEN, H. & GROSCH, C.E. 1981 The continuous spectrum of the Orr-Sommerfeld equation. Part 2. Eigenfunction expansions. *J. Fluid Mech.* **104**, 445–465.

SCHLICHTING, H. 1933 Laminare strahlausbreitung. *Z. Angew. Math. Mech.* **13**, 260–263.

SCHMID, P.J. & HENNINGSON, D.S. 2001 *Stability and Transition in Shear Flows*. Springer.

SCHUBAUER, G.B. & SKRAMSTAD, H.K. 1947 Laminar boundary-layer oscillations and transition on a flat plate. *J. Res. Natl Bur. Stand.* **38**, 251–292.

SHEIKHPOUR, M., ARABI, M., KASAEIAN, A., RABEI, A.R. & TAHERIAN, Z. 2020 Role of nanofluids in drug delivery and biomedical technology: methods and applications. *Nanotechnology Sci. Applics* **13**, 47–59.

SIDIK, N.A.C., YAZID, M.N.A.W.M. & MAMAT, R. 2015 A review on the application of nanofluids in vehicle engine cooling system. *Intl Commun. Heat Mass Transfer* **68**, 85–90.

SMITH, F.T. 1979 On the non-parallel flow stability of the Blasius boundary layer. *Proc. R. Soc. Lond. A* **366**, 91–109.

SMITH, F.T. 1989 On the first-mode instability in subsonic, supersonic or hypersonic boundary layers. *J. Fluid Mech.* **198**, 127–153.

TAYLOR, R., COULOMBE, S., OTANICAR, T., PHELAN, P., GUNAWAN, A., LV, W., ROSENGARTEN, G., PRASHER, R. & TYAGI, H. 2013 Small particles, big impacts: a review of the diverse applications of nanofluids. *J. Appl. Phys.* **113**, 011301.

TOLLMIEN, W. 1933 Uber die Entstehung der turbulenz. *Nachr. Ges. Wiss. Göttingen Math. Phys. Klasse* **II**, 21–44.

TREFETHEN, L.N. 2000 *Spectral Methods in MATLAB*. SIAM.

TURKYILMAZOGLU, M. 2014 Nanofluid flow and heat transfer due to a rotating disk. *Comput. Fluids* **94**, 139–146.

TURKYILMAZOGLU, M. 2016 Flow of nanofluid plane wall jet and heat transfer. *Eur. J. Mech. B Fluids* **59**, 18–24.

TURKYILMAZOGLU, M. 2020 Single phase nanofluids in fluid mechanics and their hydrodynamic linear stability analysis. *Comput. Meth. Programs Biomed.* **187**, 105171.

WANG, X.Q. & MUJUMDAR, A.S. 2008*a* A review on nanofluids - part I: theoretical and numerical investigations. *Braz. J. Chem. Engng* **25**, 613–630.

WANG, X.Q. & MUJUMDAR, A.S. 2008*b* A review on nanofluids - part II: experiments and applications. *Braz. J. Chem. Engng* **25**, 631–648.

WASAIF, A. 2023 Study of natural and mixed convection flow of nanofluid. PhD thesis, The University of Manchester, Manchester, UK.

WONG, K.V. & LEON, O.D. 2010 Applications of nanofluids: current and future. *Adv. Mech. Engng* **2010**, 519659.

YACOB, N.A., ISHAK, A. & POP, I. 2011 Falkner–Skan problem for a static or moving wedge in nanofluids. *Intl J. Therm. Sci.* **50**, 133–139.